Understanding the compound seismic signature of CO_2 injection in a thin carbonate reservoir during enhanced oil recovery

by

Zachary Ward Van Ornam

A.S., Onondaga Community College, 2014
B.A., State University of New York College at Geneseo, 2016

A THESIS

submitted in partial fulfillment of the requirements for the degree

MASTER OF SCIENCE

Department of Geology
College of Arts and Sciences

KANSAS STATE UNIVERSITY
Manhattan, Kansas

2020

Approved by:

Major Professor
Dr. Abdelmoneam Raef

Copyright

Abstract

This study focuses on isolating the seismic signature of supercritical CO_2 injected into a thin (below temporal seismic resolution) oomoldic carbonate reservoir, the Plattsburg Formation of the Lansing Kansas City Group, during a pilot enhanced oil recovery program utilizing supercritical CO_2 as the primary enhanced oil recovery agent. The program was monitored by a series of time-lapse seismic surveys in which a baseline survey was conducted prior to CO_2 injection with monitor surveys following in approximately two to three month intervals. A weak time-lapse anomaly between the baseline and monitor surveys allowed for successful tracking of the CO_2 front in the reservoir. However, quantitative interpretation has been challenged by the low compressibility of the reservoir reducing the fluid effect as well as tuning in the seismic signal resulting from the thinness of the reservoir (about 5 m). The data was detuned by employing time thickness and amplitude curves produced by a wedge model utilizing a representative wavelet extracted from the data. Subsequent fluid replacement modeling utilizing Gassmann's equations predicts a 1.85% decrease in seismic impedance and an ~8% change in horizon amplitude at the reservoir level of the seismic data. This change is of insufficient magnitude to be observable in difference maps and is smaller than an approximate 15% noise component of the seismic data spectrum. This, in essence, means that the background noise in the seismic data likely far exceeds the signal containing the fluid response at the reservoir level and in turn the fluid-related time-lapse seismic signature cannot be interpreted quantitatively.

Table of Contents

List of Figures

List of Tables

Acknowledgements

- Dr. Raef – for accepting me as a graduate student and allowing me to attend K-State. I've very much enjoyed my time working with Dr. Raef and appreciate his approach of providing just enough guidance for me to resolve a problem independently. I've learned a tremendous amount under his supervision and have developed a skillset that will serve me well in the workforce.
- MS Thesis committee – Dr. Totten and Dr. LaCroix – for their guidance over the course of my research.
- Dr. Kempton – for her fantastic advice on editing this report.
- Bill Barrett – for his financial support during my time at K-State as a graduate student.
- K-State Geology Department – for providing me with a teaching assistantship, without which I would not have been able to attend K-State.
- Kansas Geological Survey – for providing access to the core samples from the Hall-Gurney CO_2 enhanced oil recovery pilot program.
- IHS Markit – for donating licenses to their Kingdom and Petra software suites.
- dGB Earth Sciences – for donating licenses to OpendTect Pro.

Dedication

This work is dedicated to my mother and father who have instilled in me a strong work ethic and who's support has allowed me to discover a passion for geophysics.

Chapter 1 - Introduction

CO_2 Injection

CO_2 injection has been a subject of interest for stakeholders in the petroleum industry and regulatory agencies alike. Injection of supercritical CO_2 into depleted oil reservoirs can facilitate the recovery of hydrocarbons remaining in the reservoir after primary production and is a particularly attractive option for the geosequestration of CO_2 due to the abundance of wells and data that are often available in hydrocarbon reservoirs. CO_2 enhanced oil recovery is of particular interest as an economically feasible approach to decreasing atmospheric carbon emissions with increased oil production offsetting the costs of carbon capture (Verma, 2015).

Enhanced Oil Recovery

When an oil field is initially developed primary production from the field is driven by natural processes within the reservoir (e.g., dissolution of gases, influx of brine, reservoir subsidence, gravity) and leads to recovery rates in the range of 5%-20% of the original oil in place (Stalkup, 1984). Typically, the reservoir will then undergo secondary recovery which entails water and/or gas injection to maintain reservoir pressure which increases the recovery to 20%-40% (Stalkup, 1984). Tertiary production or enhanced oil recovery may then be carried out with the goal of sweeping residual oil in the reservoir towards production wells and can increase the total recovery of the original oil in place (Verma, 2015).

When utilized as an enhanced oil recovery agent, it is preferable to inject CO_2 above its critical pressure of 73.82 kPa and critical temperature of 31.1 °C as this ensures that the CO_2 is in its supercritical state (Verma, 2015). Supercritical CO_2 exhibits a density similar to a liquid while possessing an especially low viscosity in the range of 0.05-0.08 cP (Verma, 2015). Supercritical CO_2 is more effective at removing residual oil than gaseous CO_2, because of its

increased density, though its low viscosity negatively affects sweep efficiency (Jarrell et al., 2002). When reservoir conditions are maintained above the critical pressure and temperature (which is desirable during supercritical CO_2 enhanced oil recovery), supercritical CO_2 will undergo dissolution in oil, thus lowering the viscosity, interfacial tension and swelling the oil, resulting in an improved recovery of residual oil in the reservoir (Verma, 2015).

An important factor to consider when designing a supercritical CO_2 enhanced oil recovery program is the minimum miscibility pressure of the reservoir. Above the minimum miscibility pressure, the supercritical CO_2 will mix with the reservoir oil to form a single-phase fluid through a combination of three hydrocarbon miscible mechanisms (Stalkup, 1983). In the past minimum miscibility pressure has been defined as the reservoir pressure at which 80% of original oil in place is recovered (Holm and Josendal, 1974) and presently as the reservoir pressure at which 90% of the original oil in place is recovered (Yellig and Metcalfe, 1980). Minimum miscibility pressure is best determined by slim-tube recovery tests in a lab setting, though mathematical models and correlations are often utilized as a more economical method of approximating the reservoir minimum miscibility pressure (Verma, 2015). Above the minimum miscibility pressure, supercritical CO_2 injected into the reservoir will develop a transition zone with intermediate and higher molecular weight hydrocarbons vaporizing into the CO_2 (vaporization gas-drive) in the vicinity of the injector well and with supercritical CO_2 dissolving into reservoir oil (condensation gas-drive) farther from the injection well (Merchant, 2010). Below the minimum miscibility pressure, supercritical CO_2 and reservoir oil will not form a single-phase fluid, however supercritical CO_2 will still enter dissolution in the oil, lowering the viscosity and causing oil swelling which will improve recovery (Martin and Taber, 1992).

Design of enhanced oil recovery programs must take into account the geologic properties of the reservoir, well spacing and injection routine (Verma, 2015). For heterogenous reservoirs, variations of the normal five-spot pattern (four injection wells at the corners and a production well located at the center) or inverted five-spot pattern (four production wells at the corners and an injection well located at the center) are widely used (Verma, 2015). Water flooding may be conducted prior to supercritical CO_2 injection to raise the reservoir pressure above the minimum miscibility pressure. Continuous CO_2 injection may be used in reservoirs dominated by medium to light oil as well as in reservoirs that are strongly water-wet or sensitive to water flooding (Jarrell et al., 2002). supercritical CO_2 may also be injected in a water-alternating-gas pattern in which slugs of supercritical CO_2 followed by slugs of water are injected into the reservoir to reduce fingering of supercritical CO_2 caused by its low viscosity, thus improving sweep efficiency (Jarrell et al., 2002).

Geosequestration

Geologic storage of captured CO_2, otherwise known as geosequestration, is a promising method of curtailing CO_2 emissions with many depleted oilfields and large regional saline aquifers such as the Ozark Plateau aquifer system located near CO_2 emission sources. The Ozark Plateau aquifer system alone is capable of storing several hundred years of present level CO_2 emissions with residence times in the range of millions of years (Carr et al., 2005). Emission sources in the industrial and electric power sectors are excellent candidates for carbon capture and storage programs, because large volumes of CO_2 are generated at the point sources that these sectors consist of. In 2018, the CO_2 emissions of the industrial and electric power sectors in the United States accounted for 1003 MMT and 1763 MMT or 19.0% and 33.5%, respectively, of CO_2 emissions for the year (DOE, 2019) (p. 205-209). However, such programs require that

attention be paid to the structural, petrophysical and hydrologic properties of the target formation before initiating a geosequestration program to ensure that CO_2 is contained within the formation (Ohl and Raef, 2014). These properties are often well defined in oil and gas reservoirs and poorly defined in deep saline aquifers where an absence of well control exists (Carr et al., 2005; Ohl and Raef, 2014). Some work has been completed on developing a workflow utilizing geophysical well logs to identify lithologic facies in 3D seismic reflection data. This would allow for the training of an artificial neural network to identify petrophysical properties in oil fields with good well control and possibly the extrapolation of the artificial neural network to deeper regional saline aquifers with poor well control. This could achieve the goal of creating fluid flow models for predicting the behavior of CO_2 injected into these aquifers (Ohl and Raef, 2014).

Benefits of Combined Geosequestration and Enhanced Oil Recovery

The benefits of combining the goals of curtailing CO_2 emissions through geosequestration with those of supercritical CO_2 enhanced oil recovery cannot be ignored. The U.S. Energy Information Administration estimated that there were approximately 380,000 stripper oil wells in the U.S. in 2015 (Perrin, 2016). These are marginal wells in depleted oil fields producing no more than 15 barrels of crude per day; they accounted for ~10% of U.S. oil production for 2015 (Perrin, 2016). The sheer number of these wells would mean that geosequestration programs can proceed with exceptional well control in the target reservoirs and without the need to devote resources to the drilling of new wells for the sole purpose of sequestration. This would also represent an immense economic opportunity to stimulate production in oilfields that have not yet undergone tertiary production and still have a significant portion of original oil in place that is yet to be recovered. The sale of captured CO_2 for the purpose of enhanced oil recovery programs would also yield the benefit of reducing the reliance

of current sequestration efforts on government subsidies and would likely result in more CO_2 being captured as a result of economic incentives for investing in the necessary equipment.

Time-Lapse Seismic

4D seismic (time-lapse seismic) is a powerful tool for monitoring reservoir fluids during enhanced oil recovery operations. 4D seismic data consists of multiple 3D seismic surveys (a baseline survey and a number of monitor surveys) that have been gathered with some amount of time separating the 3D surveys. A necessary component, and perhaps the biggest challenge of 4D seismic, is repeatability. That is, the 3D surveys in a 4D dataset must be collected under identical conditions in order to eliminate changes between surveys that are due to factors other than those related to production within the target reservoir (Calvert, 2005, p. 4).

Some of the earliest commercial applications of 4D seismic data occurred in the 1980s, producing results that were primarily qualitative in nature due to difficulties in achieving sufficient repeatability (Hirsche, 2006). Later development in the 1990s and early 2000s shifted the focus to tracking and quantifying fluid and pressure changes, eventually leading to an emphasis on utilizing 4D seismic as a primary component of reservoir management programs (Walker and Parr, 2007). Marine settings are ideal for the acquisition of 4D seismic data because of a typically small random noise component compared with terrestrial data as well as conditions that simplify the repeatability of survey geometry. Tertiary settings generally possess more sources of unrepeatable noise as well as more complex velocity regimes, particularly in the shallow subsurface. In general, this means that tertiary reservoir management programs are more complicated in terms of seismic data acquisition and processing than marine counterparts.

CO_2 Effect on Time-Lapse Anomaly

When CO_2 is introduced into a reservoir the seismic properties of that reservoir are altered. The degree of this alteration is dependent upon the amount of CO_2 injected into the reservoir as well as the properties of the rock matrix. These effects mean that time-lapse seismic can be a powerful tool for monitoring CO_2 injection programs.

In a landmark study conducted by Arts et al. (2002), supercritical CO_2 was injected into the Utsira Sand, a loosely consolidated sandstone of the Sleipner field in the North Sea. A baseline 3D seismic survey was conducted in 1994 prior to CO_2 injection and a monitor 3D seismic survey was collected in 1999 following three years of CO_2 injection over which 2.28 MT of CO_2 were injected into the reservoir. The loosely consolidated matrix of the Utsira Sand yielded a significant drop in seismic velocity and change in amplitude between the baseline and monitor survey, even in portions of the reservoir with only a moderate CO_2 saturation. Arts et al. (2002) utilized Gassmann's fluid replacement equations to estimate the velocity change due to CO_2 saturation of the reservoir. This velocity was then used to calculate a corresponding volume of injected CO_2. The process was repeated for a variety of CO_2 densities corresponding to the pressure and temperature conditions of the reservoir, as well as a variety of reservoir porosities within the range observed by well logs to produce a range of estimated volumes of CO_2 in the reservoir. These estimated volumes could then be compared to the known volume of CO_2 injected into the reservoir and used to refine the reservoir parameters in the estimation.

Challenges of Applying Time-Lapse Seismic in Carbonate Reservoirs

Carbonate reservoirs pose a challenge for time-lapse seismic because the high rigidity of carbonate rock frames tends to diminish the expression of changes in reservoir fluid and reservoir pressure in seismic data. Further, due to complicated diagenetic processes, carbonates exhibit a broad degree of heterogeneity that lends to uncertainty in the distribution of porosity and permeability in the reservoir. The acquisition, processing and interpretation of seismic data targeting carbonate reservoirs is challenged by this heterogeneity and is still not as well understood as in siliciclastic settings, despite carbonate reservoirs comprising more than half of global hydrocarbon reserves (Palaz and Marfurt, 1997).

Carbonates exhibit a wide array of porosities ranging from interparticle, intraparticle, moldic and vuggy that arise from a combination of primary and secondary diagenetic processes. The aspect ratio of pores can be utilized as a tool to quantitatively describe pore geometry (Xu and Payne, 2009). This metric takes the ratio of the length of the short axis to the length of the long axis of a pore and can be inverted from seismic data (Xu and Payne, 2009). Xu and Payne (2009) found that P-wave velocities can vary by up to 40% for a given porosity from variation in pore geometry alone, with high aspect ratio pore geometries such as moldic, intraframe and vuggy supporting higher P-wave velocities and low aspect ratio pores, such as microcracks and fractures, reducing P-wave velocity. This further complicates the task of isolating fluid effects on seismic velocity and necessitates the need to understand the spatial variation of porosity when conducting time-lapse seismic surveys of carbonate reservoirs.

In addition to complex velocity profiles arising from pore geometry, carbonates possess additional characteristics that pose a challenge to resolving carbonate reservoirs in reflection seismic data. Carbonate platforms produce complicated structures in the subsurface marked by steeply dipping reflectors on the flanks of the platform, which can pose challenges to the

processing of the seismic data (Sarg and Schuelke, 2003). Additionally, a low contrast in acoustic impedance between carbonate horizons with similar mineralogies can make it difficult to resolve oil-bearing carbonates from overlying tight carbonate seals (Skirius et al., 1999). Evaporite deposits that are associated with the deposition of carbonates can scatter and attenuate the energy of the downgoing wavelet, decreasing the ability to resolve reflectors below the evaporite horizon (Skirius et al., 1999). The high interval velocity of carbonates relative to siliciclastic horizons can lead to multiples in the seismic data, which will need to be removed in the processing of the dataset (Sarg and Schuelke, 2003). In summary, the heterogeneities that are inherent to carbonate diagenesis create numerous factors other than changes in reservoir fluid and pressure that can affect the expression of carbonates in time-lapse seismic datasets.

Seismic Resolution and Tuning

When interpreting seismic data, it is paramount to consider the resolution of the dataset. Seismic resolution can be considered in two directions, lateral and vertical. The bandwidth of the dataset is perhaps the most important factor controlling the resolution in both of these directions; however, the accuracy of the velocity model for migrated seismic as well as the sampling interval are also important factors (Simm and Bacon, 2014).

To understand the lateral resolution of seismic data, the region of the downward propagating wavefront, referred to as the Fresnel zone, must be considered. Reflection events in the seismic data are the result of constructive interference over the Fresnel zone (Sheriff, 1977). For unmigrated seismic data, Sheriff (1977) defined the diameter of the Fresnel zone (F_d) according to the following equation:

Equation 1-1: Diameter of the Fresnel zone in reflection seismic data

$$F_d = 2\sqrt{\left(z + \frac{\lambda}{4}\right)^2 - z^2}$$

where λ = wavelength and z = depth. Migration collapses the Fresnel zone to approximately half the wavelength and is a crucial component of enhancing lateral resolution in seismic data (Simm and Bacon, 2014).

Vertical resolution in seismic data is controlled by a phenomenon referred to as tuning. Tuning, in its simplest form, occurs when the energy reflected from the base of a horizon overlaps and thus interferes with the energy reflected from the top of the horizon. This causes the amplitude of the reflection event to deviate from the natural seismic response to contrast in acoustic impedance. Widess (1973) describes tuning effects for a progressively thinning layer (Figure 1-1) in which the onset of tuning occurs when the thickness of the layer is equal to half the wavelength (λ/2) of the down-going signal. Constructive interference between the signal from the top and base of the layer increases until the layer thickness is equal to one quarter of the wavelength (λ/4); this is referred to as maximum tuning thickness. Destructive interference then increases until the layer thickness is equal to one eighth of the wavelength (λ/8); this is considered to be the theoretical threshold of vertical resolution and any features less than λ/8 cannot be uniquely resolved in the seismic data.

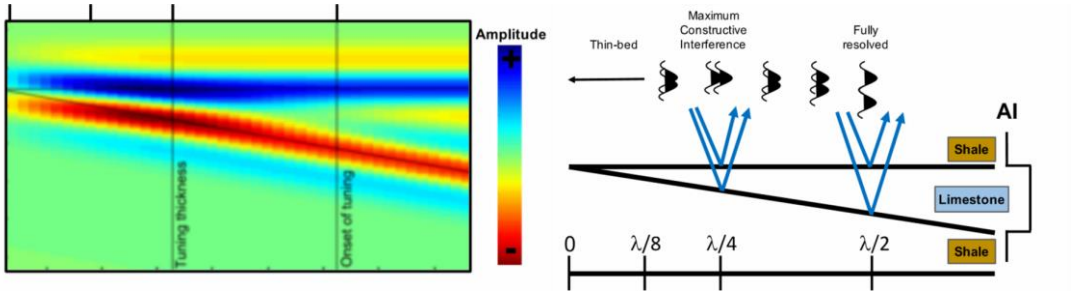

Figure 1-1: Wedge model for a thinning limestone reservoir bound by upper and lower shale beds. When the reservoir thickness is λ/2 the confining layers and the reservoir are fully resolved. Thickness values less than λ/2 are affected by tuning, with maximum constructive interference occurring when the reservoir thickness is λ/4. The reservoir is unresolvable when the thickness is less than λ/8. (Modified after Agile Geoscience, 2011)

Chapter 2 - Background

CO_2 Pilot Program

On March 8, 2000, the National Energy Technology Laboratory of the Department of Energy (DOE) began a pilot project to determine the economic and technical feasibility of implementing a miscible CO_2 flood to recover oil bypassed during the primary production of the Plattsburg formation, an oomoldic limestone of the Lansing Kansas City (LKC) Group, which is located at an approximate depth of 2,900 ft (NETL, 2010). The pilot project was conducted in the Carter-Colliver lease of the Hall-Gurney field (Figure 2-1) using one injector well and two production wells (Figure 2-2) (NETL, 2010). Injection of miscible CO_2 began on December 2, 2003, and continued through June 21, 2005, when injection was transitioned to water with a total of 16.9 MM lb of CO_2 injected into the reservoir (NETL, 2010). By March 7, 2010, 8,736 bbl of oil were produced from the pilot and 19,166 bbl of oil were produced from the adjacent leases Colliver A8, Colliver A3, Colliver A14 and Graham A4 (NETL, 2010). Total oil recovery attributed to CO_2 injection is 27,902 bbl, with a miscible CO_2 sweep efficiency of 4.8 MCF/bbl, causing the pilot program to be uneconomic (NETL, 2010).

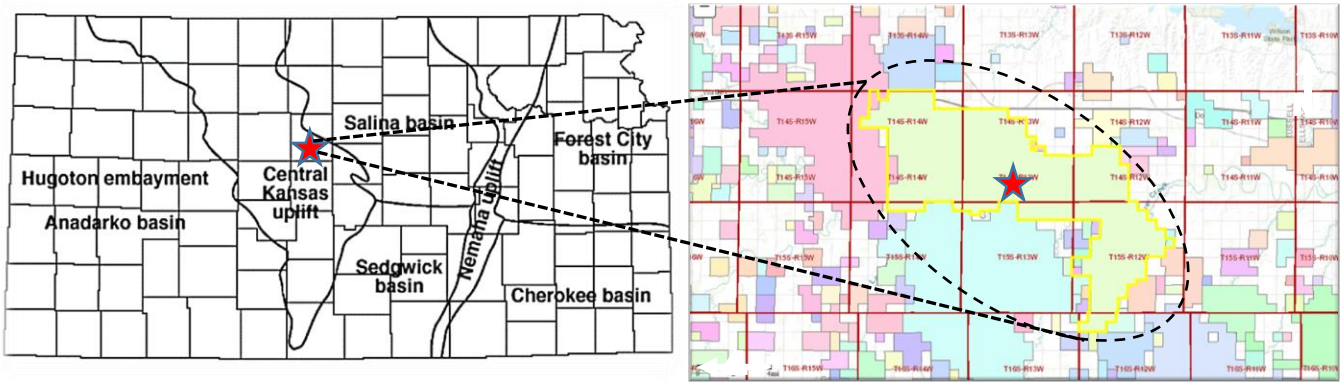

Figure 2-1: (A) Uplifts and basins of Kansas. The CO_2 pilot program is located in Russell County, within the Hall-Gurney field on the Central Kansas uplift, as indicated by the red star (Modified from Baars et al., 1993). (B) The Hall-Gurney field, highlighted in yellow and shaded in green. The pilot program is located at the red star (Modified from KGS, 2011).

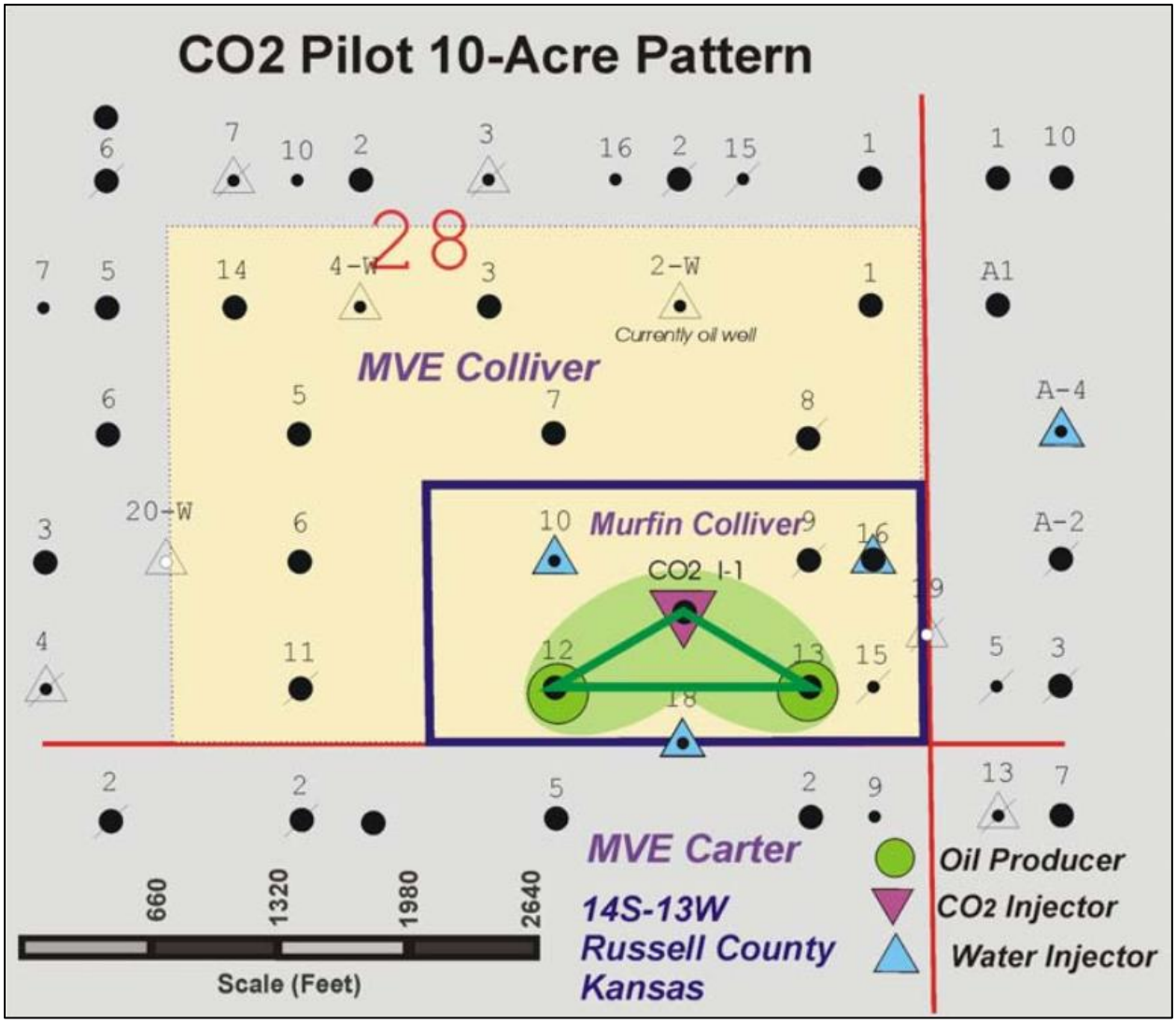

Figure 2-2: The CO_2 pilot pattern, located within the blue rectangle (from Raef et al., 2005a). The region shaded in green depicts the predicted CO_2 sweep pattern while the green lines linking the CO_2-I and Colliver 12 and 13 wells depicts communication between these wells. This was later proven to be false when CO_2 was only produced from the Colliver 12 well and the migration of the CO_2 off lease to the north (Figure 2-3d) resulting in the early termination of the pilot program. All wells in section 28, township 14S, range 13W, Russell County are plotted on this map with symbol size representing cumulative production relative to other wells in view.

Eight 3D seismic surveys were acquired by the Kansas Geological Survey (KGS) over the course of the pilot program (a baseline survey and seven monitor surveys) for compilation into a 4D (time-lapse) seismic dataset. The baseline survey was recorded prior to CO_2 flooding

while the first monitor survey (M1) was recorded two months after CO_2 injection commenced. Monitor surveys were acquired every two to three months, while the fifth monitor survey (M5) was recorded after approximately 13 months of CO_2 injection.

Progressively Parallel Blanking

Raef et al. (2005a) successfully utilized progressively parallel blanking, a non-differencing approach, to track CO_2 in the Russell county 4D seismic survey, in spite of a weak time-lapse anomaly that prevented the use of traditional differencing methods. Progressively parallel blanking utilizes textural, rather than magnitude, differences across surveys to track the migration of CO_2 in the reservoir and can reveal weak time-lapse anomalies, as in such cases where amplitude differences are of the same magnitude as unrepeatable noise (Raef et al., 2005a). The progressively parallel blanking method functions by setting all values within a time slice that are above or below a threshold to background color (i.e., removing them from the time slice), while all values within the threshold range are rendered in the time slice with a high-resolution color bar (Figure 2-3) (Raef et al., 2005a). This allows CO_2 to be tracked spatially using textural changes between the baseline and monitor surveys (Raef et al., 2005a).

The progressively parallel blanking method proved to be effective in tracing the subtle effect of CO_2 in the reservoir facies and was forgiving of unrepeatable noise and variations in the cross-equalization between the baseline and monitor surveys (Raef et al., 2005a). Further, the progressively parallel blanking approach maintains similarity between surveys where no time-lapse anomaly is expected (Raef et al., 2005a). However, it is a difficult process to automate and produces results that are qualitative in nature, meaning that it is impossible to attain such information as CO_2 saturation at the reservoir facies (Raef et al., 2005a).

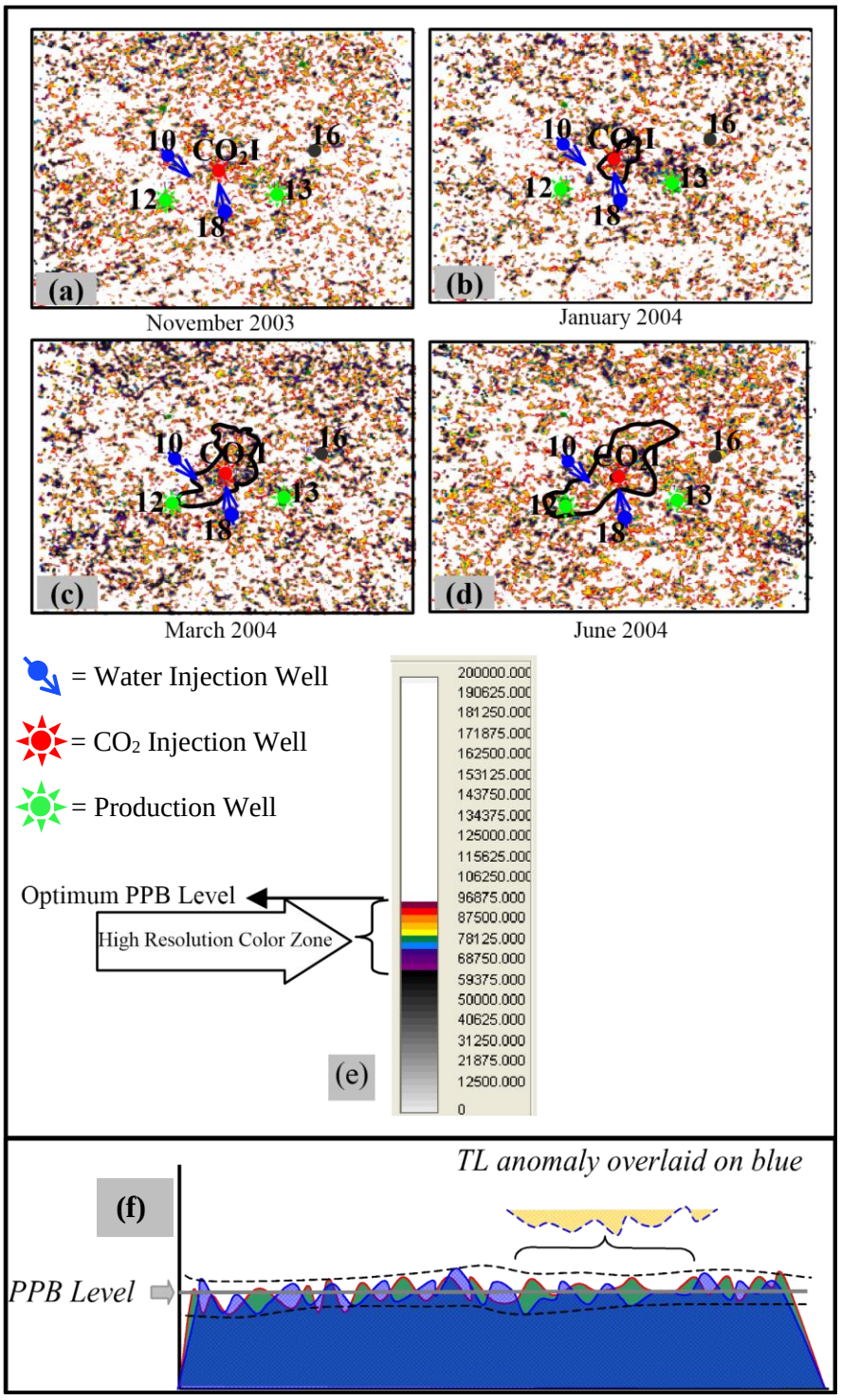

Figure 2-3: Progressively parallel blanking method applied by Raef et al. (2005a) to the (a) baseline survey, (b) the M1 survey, (c) the M2 survey (d) the M3 survey, (e) progressively parallel blanking color scale applied to baseline and time-lapse amplitude envelope horizon attribute, and (f) schematic of the progressively parallel blanking method in which the time-lapse amplitude envelope horizon attribute is calculated for each monitor survey. The areas outlined in the monitor surveys depict the interpreted extent of the CO_2 plume around the CO_2-Injector well and the Colliver 10,12, 13,16 and 18 wells.

Amplitude Envelope Analysis

Krehel (2017) conducted amplitude envelope analysis across frequency sub-bands (30-80 Hz) of the Russell 4D survey, allowing for the identification of potential shoals as well as for the analysis of potential fluid pathways and baffles within the reservoir (Krehel, 2017). These potential shoal boundaries were tracked on the LKC horizon along spatially sustained amplitude anomalies (Krehel, 2017). East-west trending lineaments were observed in the shoal boundaries and may explain the migration of the CO_2 outside the pilot program (Krehel, 2017). The seismic response to tuning was analyzed in this study, but no attempt to remove or mitigate the effect was made at the time.

Geologic Setting

Hall-Gurney Field

The Hall-Gurney Field is a 24,299-acre, primarily oil-producing field, situated in the Central Kansas Uplift geologic province. The majority of the field lies within Russell County (T14S-R14W, T14S-R13W, T14S-R12W, T15S-R14W, T15S-R13W, T15S-12W), with a small part of the southeastern portion extending into Barton County (T16S-R12W) (Figure 2-1) (KGS, 2011). The Central Kansas Uplift is a northwest-southeast trending structural high that formed between the post-Meramecian stage of the mid-Mississippian (340-355 Ma) and the Morrowan and Desmoinesian stages of the mid-Pennsylvanian (310-330 Ma) (Figure 2-1) (Merriam, 1963). This was a period of structural instability in the region, resulting from the collision of the North American and South American-African continental plates (Baars et al., 1993). It is composed of a complex series of folds and faults, forming structural/stratigraphic traps and leading to the Central Kansas Uplift being one of the most densely drilled targets in North America (Baars et al., 1993).

Depositional Environment and Regional Stratigraphy

The majority of oil and gas production in Kansas comes from rocks of Paleozoic age. These rocks generally thicken to the south and east, indicating the basin, underlain by Precambrian basement rocks, deepened towards the Oklahoma border (Baars et al., 1993). Basal nearshore sandstones of early Paleozoic age (Lamotte and Reagan sandstones) are overlain by the Arbuckle Group, a dolomite deposited in wide-ranging tidal flats during the Cambrian to the middle Ordovician (Figure 2-4), which represents the first major sea level advance and retreat recorded in Kansas stratigraphy (Baars et al., 1993).

During the Middle Ordovician to the Lower Devonian, epeiric sea level again rose in the midcontinent, as recorded by the sandstones and shales of the Simpson Group (Baars et al., 1993). Clastic sedimentation diminished as cratonic sources of mud and sand were reduced, leading to a transition to carbonate deposition, including the deposition of the Viola Limestone as well as the limestones and dolomites of the Hunton Group (Baars et al., 1993). Uplift, dropping sea level and subsequent erosion stripped much of these deposits from the Central Kansas uplift, particularly those of the Silurian-Devonian (Baars et al., 1993).

Another sea level rise in the Devonian led to the deposition of the Chattanooga shale, a primary source rock for hydrocarbon generation in the region (Baars et al., 1993). Shales were again followed by carbonate deposition and diagenesis, this time on an extensive shallow marine shelf, which exhibits numerous depositional settings, reflecting minor fluctuations in the sea level through the Devonian into the Mississippian (Baars et al., 1993). Meriam (1963) suggests that Mississippian strata were deposited over all of Kansas and eroded from areas of uplift, as an unconformity exists in the Central Kansas uplift where Upper Pennsylvanian strata are deposited atop mostly Ordovician and some Devonian rocks (Figure 2-4). In some localized areas of the

Central Kansas uplift, Upper Pennsylvanian rocks are deposited atop of Precambrian rocks, indicating the complex heterogeneity of the structural features in the region (Baars et al., 1993).

Basin subsidence occurred in the Middle and Late Pennsylvanian and Early Permian at a rate greater than the structural uplift along faults, leading to a resumption of deposition (Baars et al., 1993). The Lansing Kansas City formations of Upper Pennsylvanian age consist of oolitic limestones deposited in en echelon shoals during multiple sea level fluctuations (Byrnes et al., 2003). These sea level fluctuations were driven by glacioeustatic variation as well as regional structural instability as a result of the collision between the North American and South American-African plates (Baars et al., 1993). LKC oomoldic reservoirs were deposited across Kansas; however, they are thicker and have higher porosity at the crest or flanks of paleostructural highs, such as those underlying the Hall-Gurney Field (Byrnes et al., 2003). Interbedded carbonate muds within the LKC acted as aquitards and may have influenced the percolation of meteoric water cementation around ooids, as well as the dissolution of ooids, resulting in a vuggy porosity (Byrnes et al., 2003). Later burial led to early fracturing of oomoldic reservoirs, resulting in interconnectivity between oomolds (Byrnes et al., 2003).

Figure 2-4: A generalized stratigraphic column of Kansas stratigraphy indicating oil/gas bearing formations on the left. The region shaded in red is not present in the Central Kansas uplift due to sea level fall and subsequent erosion in the Upper Mississippian. The region shaded in green indicates the Lansing Kansas City Group, containing the most prolific reservoirs in the Central Kansas uplift as well as the Plattsburgh limestone, the target of the pilot program (Modified after Baars et al., 1993).

Plattsburgh Formation

The Plattsburg limestone, the target of the National Energy Technology Laboratory enhanced oil recovery program, is one of approximately a dozen limestones separated by shale beds within the cyclothems of the LKC Group. It was deposited in a shallow marine shelf environment (Newell et al., 1987) and is classified as a regressive oomoldic limestone of late Pennsylvanian age (Watney, 1994). Optimal reservoir conditions occurred in the ooid shoal facies on the flanks of paleostructure highs (Byrnes et al., 2003). The porosity and permeability of the Plattsburg limestone developed through extensive diagenetic overprinting resulting from subaerial exposure and percolation of meteoric water as well as through later fracturing/matrix crushing from burial (Byrnes et al., 2003).

The Plattsburg limestone is characterized by a complex pattern of stacked, cross-cutting and shingled ooid shoals resulting from reworking and redeposition of shoals during the frequent global and local sea level fluctuations of the Late Pennsylvanian-Early Permian (Byrnes et al., 2000). Watney (2015) and Watney et al. (2006), suggest the deposition of three stacked shoal complexes (Figure 2-6), illustrating the lateral heterogeneity of the Plattsburg limestone. Porosity and permeability in the reservoir are variable, with the best reservoir conditions occurring in zones with no neomorphism or where later fracturing of the oomoldic fabric has increased the permeability (Figure 2-5) (DuBois et al., 2001).

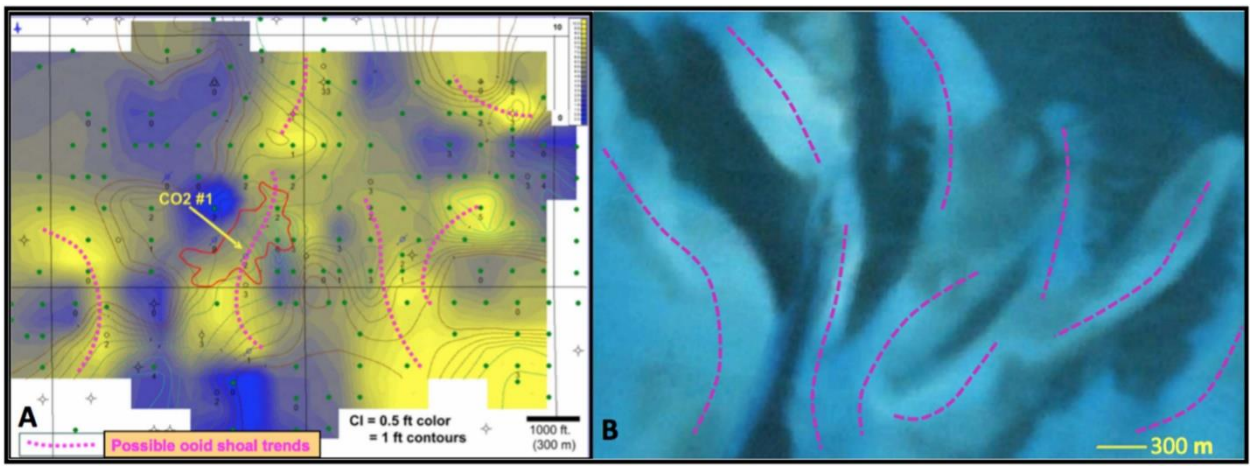

Figure 2-6: (A) An interpretation of possible stacked shoal in the Plattsburg formation on a structure map of the Plattsburgh limestone, derived from formation tops at nearby oil wells (green dots). Regions shaded in yellow represent high porosity zones while regions shaded in blue represent low porosity zones. The region encompassed by the red line depicts the extent of the CO_2 plume as interpreted by Raef et al. (2005a) (Watney et al., 2006), and (B) an analogous system in the present-day Bahamas, pictured here in satellite imagery (Google Earth, 2015). The purple dashed lines in (A) and (B) depict ooid shoal trends in map view.

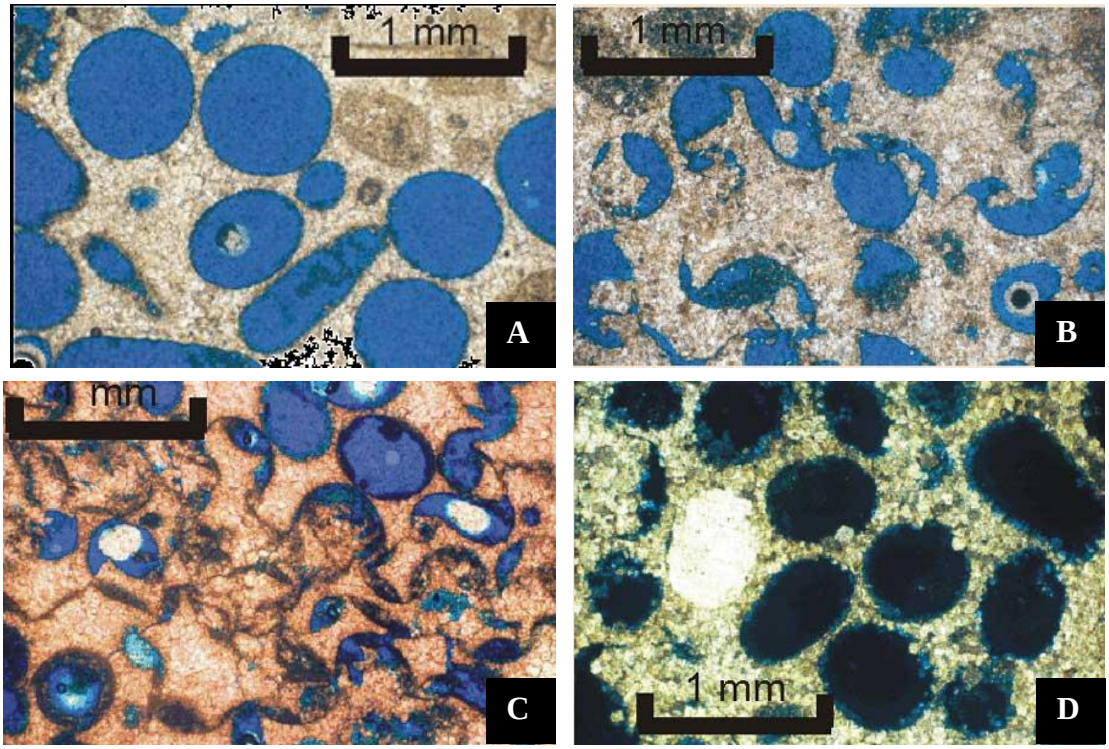

Figure 2-5: Φ = porosity, k = permeability. (A) Φ = 32.0% k = 101.0 md, oomolds with no neomorphism or crushing, (B) Φ = 32.0% k = 101.0 md, slightly neomorphosed oomolds, crushing has added permeability, (C) Φ = 29.1% k = 46.7 md, heavy crushing of the matrix has reduced porosity, but has maintained fluid pathways, and (D) Φ = 22.9% k = 5.6 md, neomorphism of oomolds has choked off fluid pathways and the absence of fractures has maintained isolation of the oomolds (from DuBois et al., 2001).

LKC Petroleum System

The Lansing Kansas City Group consists of multiple pay zones consisting of alternating layers of thin carbonate and shale beds (Higley, 1995). Within the oomoldic limestone beds of the LKC, porosities range up to 35% whereas permeabilities range from 0.001-400 md (Byrnes et al., 2003). There is debate over the origin of hydrocarbons in the LKC Group, as Pennsylvanian shales are thermally immature in the Central Kansas uplift; one model proposes hydrocarbon migration from the Anadarko basin to the south (Higley, 1995). Another model proposes that hydrocarbon generation was driven by the radioactivity of black marine shales and only considers thermogenic maturation (Kelly, 2014). Numerous anticlinal traps exist within the Central Kansas uplift, resulting from variations in fault offsets, causing localized stresses and deformations across the region (Baars et al., 1993). The interlayered shales act as seals within structural traps (Baars et al., 1993).

Chapter 3 - Data

Time-Lapse Seismic Dataset

This project utilizes the 4D seismic data acquired by KGS during the enhanced oil recovery program implemented by National Energy Technology Laboratory. Design of the survey considered repeatability, azimuthal and fold coverage, subsurface resolution and minimization of footprint (Raef et al., 2005b). These criteria were met with a modified brick, single-patch survey (Figure 3-1) with 810 source shot points and
240 receiver stations, which were positioned using differential GPS (Raef et al., 2004). Sources were spaced 100 m on north-south trending lines 1.5 km long (Raef et al., 2004) while receivers were spaced 200 m in east-west trending lines 1.0 km in length (Miller et al., 2007). An IVI Minivib II was used to produce five linear 10-second upsweeps ranging from 25-250 Hz at each shot point; the first upsweep is used to couple the pad and the latter four are used in stacking (Miller et al., 2007). Phase variations are to be expected between shots within surveys, as well as across surveys because the vibroseis was not phase locked (Raef et al., 2005b). These parameters were held constant for the baseline and seven monitor surveys (M1, M2, M3, M4, M5, M6 and M7), each consisting of 166 inlines and 175 crosslines with a bin spacing of 10 m.

For the purpose of this study, only the baseline and the M5 monitor survey will be analyzed, as the M5 survey was acquired January 2005, prior to the switch to a waterflood. The amplitude spectra for the baseline and M5 surveys are displayed in Figure 7; some of the high frequencies present in the baseline survey are attenuated in the M5 survey, shifting the dominant frequency slightly towards the lower end of the spectrum. This could be due to an unaccounted-for variation in the data acquisition between the baseline and M5 survey, or possibly due to CO_2 saturation.

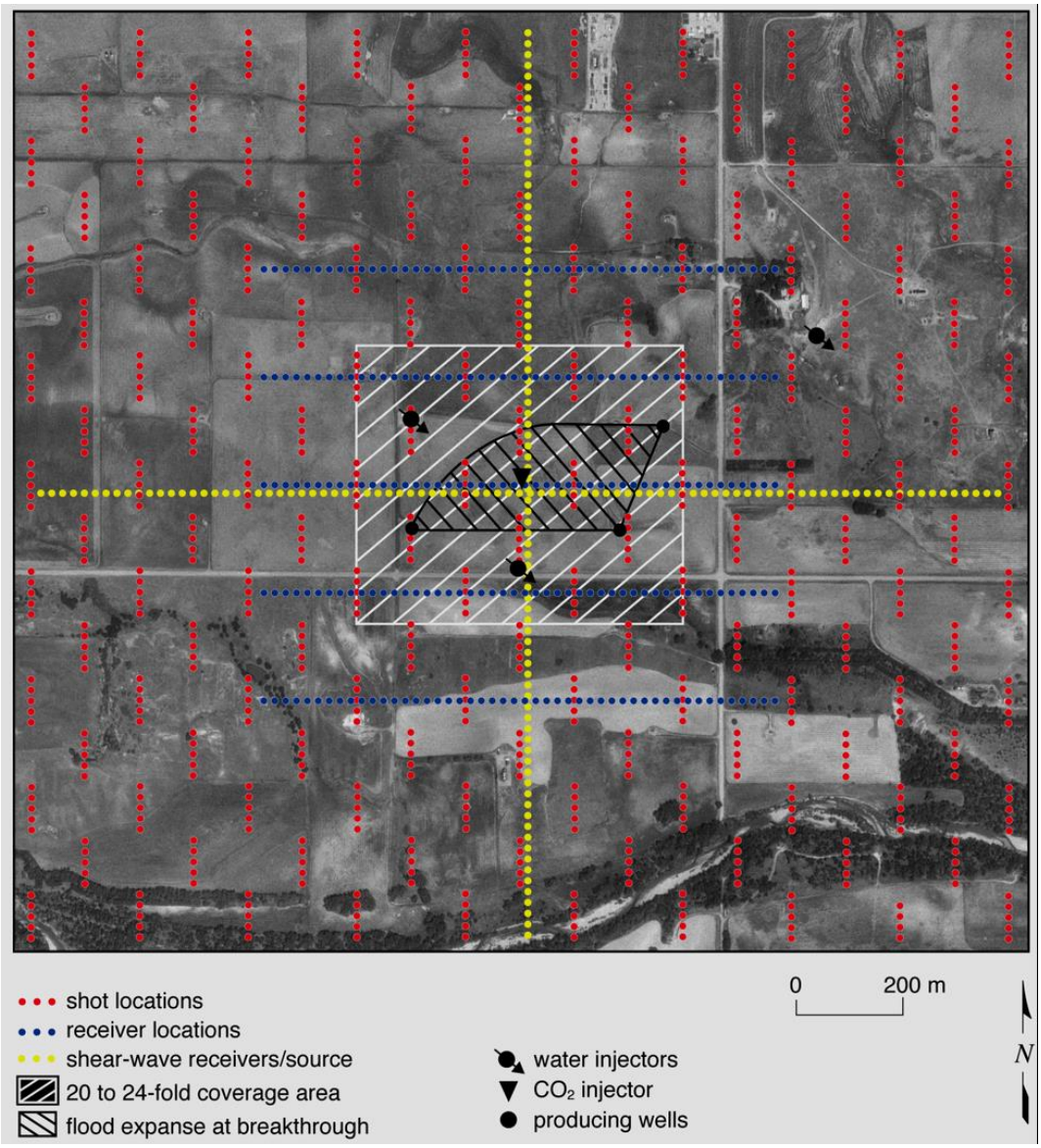

Figure 3-1: Map view of the 3D seismic survey design showing N-S trending shot locations (red), E-W trending receiver lines (blue), and shear-wave receivers/sources (yellow) (from Raef et al., 2004). The shear-wave data was unavailable for this study.

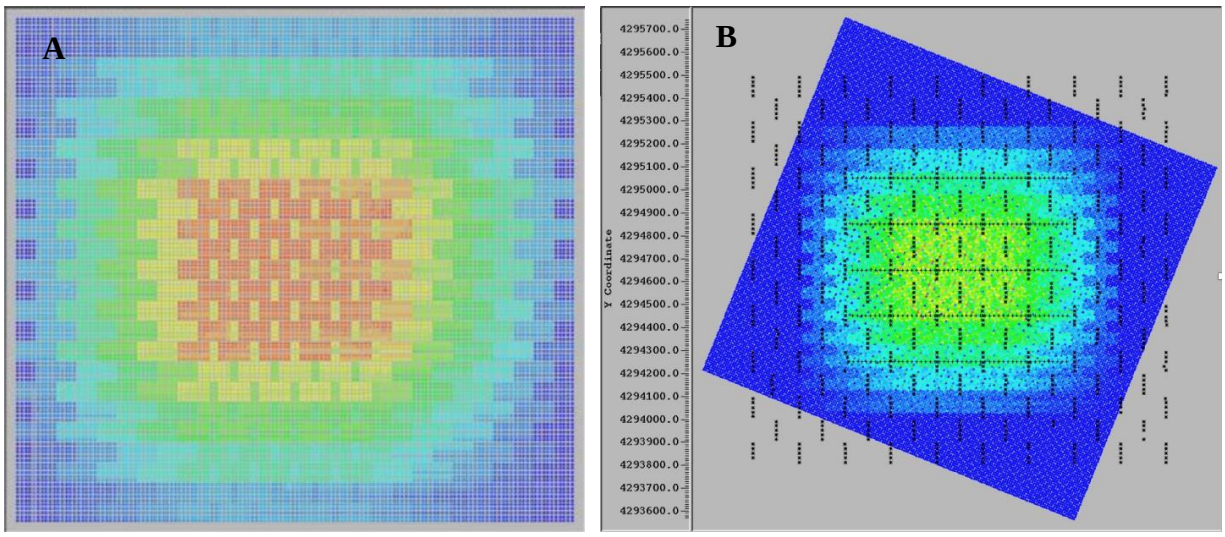

Figure 3-2: (A) Fold of coverage prior to grid rotation, and (B) resulting fold of coverage after a 112° grid rotation was applied to improve the fold distribution in the central area of the survey. Red = 24-fold and yellow = 20-fold (from Miller et al., 2007).

Import Parameters

Table 3-1: 3D seismic survey import parameters

IEEE floating point; Z-range = 0-801 ms with 1 ms step interval; 10 m bin spacing; Seismic reference datum = 485 m			
NAD27, UTM Zone 14N (OpendTect); NAD27, Kansas North (IHS Kingdom)			
Line	Trace	X Coordinate (m)	Y Coordinate (m)
1	1	519746.00	4295747.00
1	175	521359.00	4295095.00
166	175	520741.00	4293565.00

Well Data

Six wells are present in the area covered by the 4D seismic dataset; these include one CO_2 injector (CO2-I #1), two water injectors used for pressure containment (#10 and #18), two producers (#12 and #13) and one monitoring well (#16) (Figure 2-2). Table 3-2 summarizes the information pertaining to these wells.

Table 3-2: Hull-Gurney CO_2 enhanced oil recovery pilot program well data.

Well	Unique Well Identifier	Type	Surface X (m)	Surface Y (m)	Kelly Bushing Elevation (m)	Total Depth (m)
CO2-I #1	15-167-23179	CO_2 + Water Injector	520266.90	4294431.10	528.22	949.45
#10	15-167-02488	Water Injector	520065.20	4294531.50	530.05	911.96
#12	15-167-19056	Producer	520062.20	4294329.60	525.48	900.96
#13	15-167-02513	Producer	520467.70	4294331.70	524.26	900.68
#16	15-167-02515	Monitor	520568.10	4294533.00	528.52	905.56
#18	15-167-03186	Water Injector	520267.40	4294242.40	525.78	914.40

Table 3-3: Hull Gurney CO2 enhanced oil recovery pilot program well formation tops.

	Wells					
Formation Tops	CO2-I #1	#10	#12	#13	#16	#18
Heebner Shale top (m)	851.00	851.31	848.72	848.41	847.96	847.96
Lansing Kansas City (LKC) top (m)	868.93	871.73	869.29	869.90	873.02	868.68
Lansing Kansas City C-Zone (LKCC) top (m)	881.03	883.31	879.81	879.81	878.43	878.74
Lansing Kansas City D-Zone (LKCD) top (m)	886.97	887.88	885.14	885.92	883.92	883.31

Chapter 4 - Methodology

Software Used in This Study

The table below provides a list of the software and respective software versions utilized in this study.

Table 4-1: Software used in the workflow and analysis of this study.

Software and Version Information
IHS Markit Kingdom, Version: 2019 – 64-bit, 13.0 Build: 120 (May 22, 2019)
dGB Earth Sciences OpendTect, Version: 6.4.4 (May 26, 2019), 64-bit
MathWorks MATLAB R2015b (8.6.0.267246) (August 20,2015), 64-bit
Microsoft Excel, Version: 1910, Build: 12130.20272, 64-bit
GCTS C.A.T.S. Ultrasonics rvC, Version: 1.89

Preparation of the Seismic Data

Wavelet Extraction

Zero-phase wavelets were extracted for the baseline and fifth monitor surveys (Figure 4-1) for a 150 meter radius around the CO2-I #1 well, encompassing 684 traces. A time window ranging from 0.310-0.670 seconds was utilized as this depth range encompasses the LKC Group and excludes zones of incoherency in the upper and lower extents of the data. These wavelets are used to generate synthetic seismograms for creating a well-to-seismic-tie and conduct tuning analysis on the baseline and fifth monitor survey.

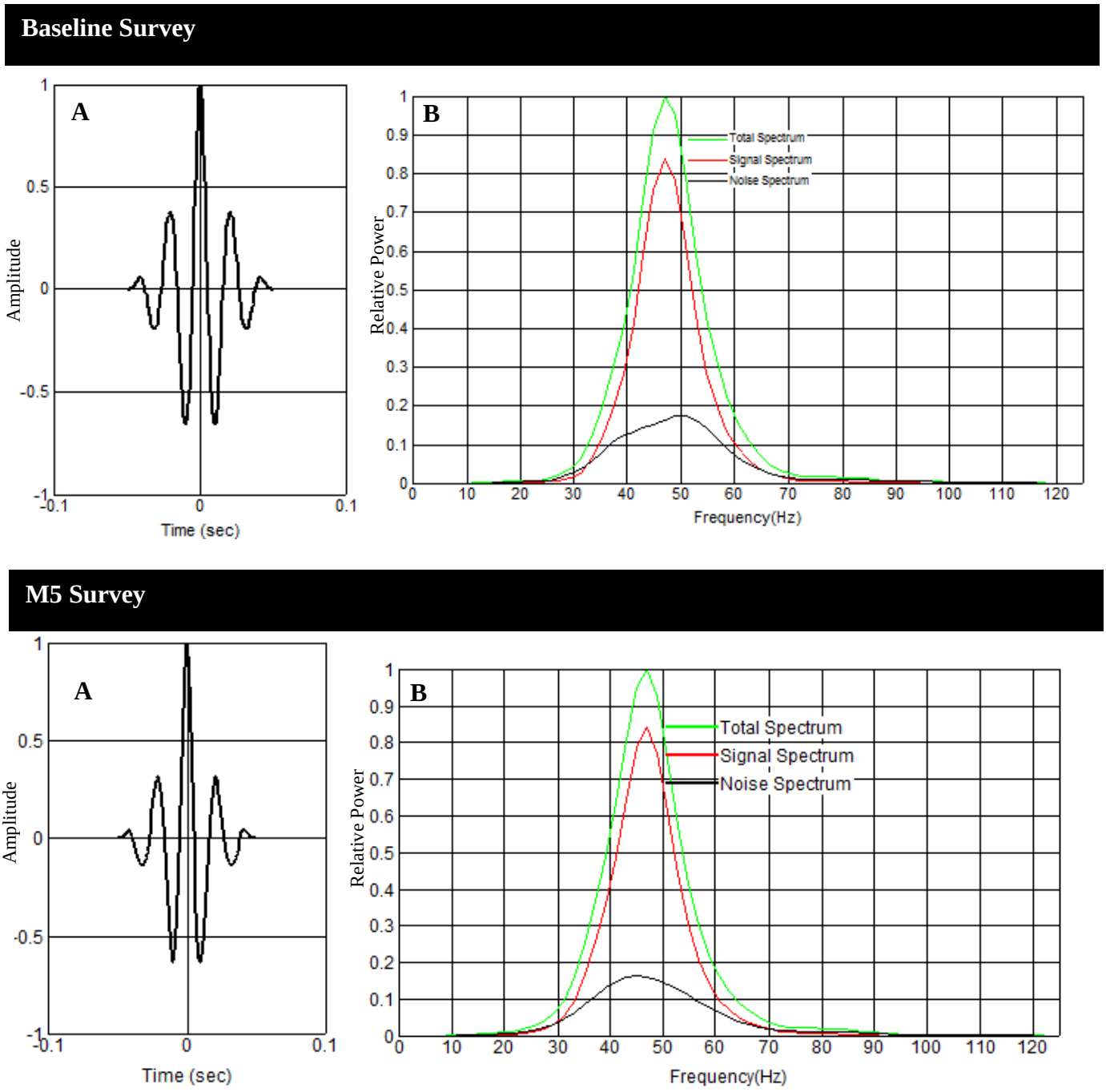

Figure 4-1: (A) Wavelet extracted from the baseline and M5 surveys around the CO2-I #1 well through the reservoir interval, and (B) Total, Signal and Noise spectrums of the extracted wavelets. This operation was completed using the frequency matching method in the Wavelet Wizard Tool in IHS Kingdom. Note that approximately 15% of the survey spectrum of the baseline and M5 surveys over the primary frequency components of the data (40-55 Hz) consist of noise. It then follows that CO_2 must have a time-lapse effect in excess of 15% in order to be discernable.

Well-to-Seismic-Tie

A synthetic seismogram is the result of forward modelling of seismic response in which sonic and density logs are utilized to create a reflection coefficient series which is convolved with a wavelet to create a synthetic seismic image. This synthetic image is then matched to the seismic data in order to create a velocity model which may then be used to match reflection events to formation tops at the well and transform the data to depth domain.

The sonic and formation density logs from the CO2-I #1 well and the wavelet extracted from the baseline survey were used in the creation of a synthetic seismogram which was matched to the baseline survey. The well logs were edited to remove spikes and the depth range was limited to 631 m to 954 m in order to remove noise and avoid matching to zones of low coherency in the seismic data (Figure 4-2). A bulk shift was applied to the synthetics to match prominent reflectors based on reflection strength and character. Only minor stretches/squeezes were applied to match prominent reflectors in order to maintain a plausible velocity model. A final cross-correlation coefficient of 0.825 was achieved (Figure 4-3). The resulting time-depth table was shared with the monitor surveys.

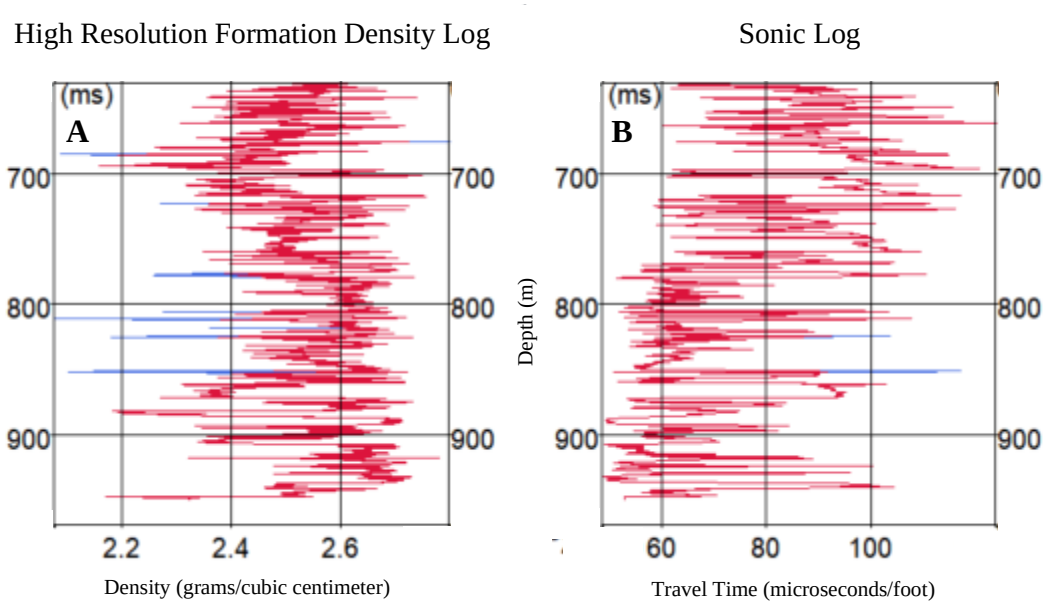

Figure 4-2: (A) Edited high resolution formation density, and (B) sonic logs at the CO2-I #1 well. The sections of the curve highlighted in blue were removed with a de-spiking filter using a 300 sample window size with a Grubbs number threshold of 3.00; spikes were replaced with interpolated values. This procedure was completed with the log editor tool in OpendTect.

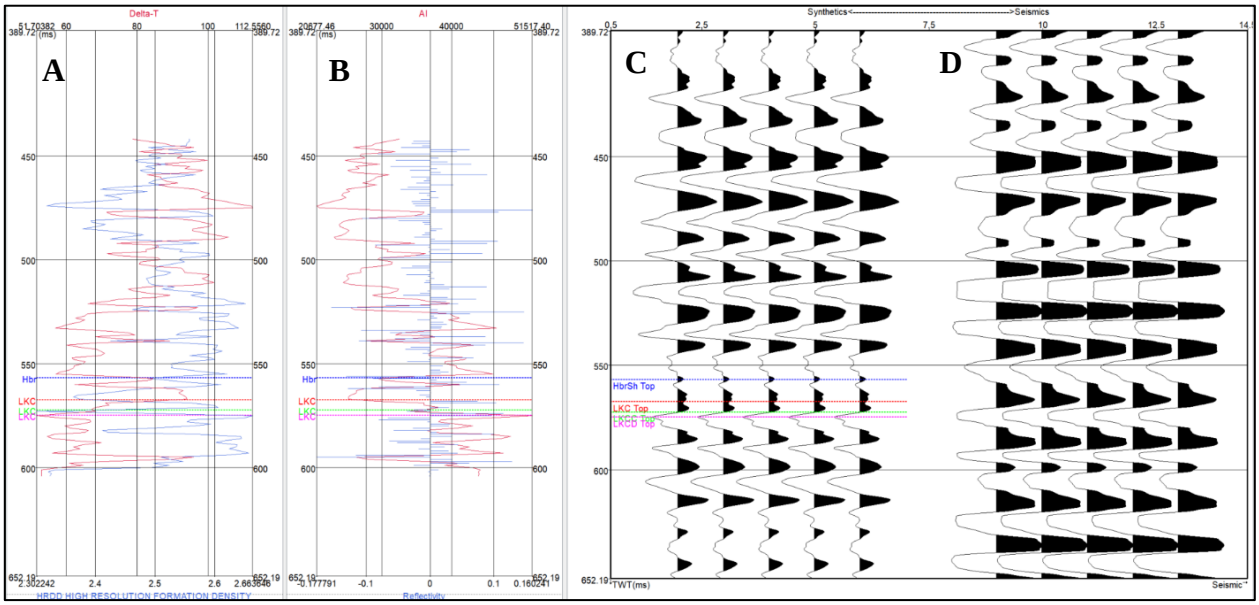

Figure 4-3: (A) Sonic log in red, high resolution formation density log in blue, (B) acoustic impedance in red, reflectivity series in blue, (C) synthetic seismogram, and (D) seismic data. The reflectors in the synthetic seismogram (C) were matched to the reflectors in the seismic data (D) on the basis of reflection strength and character. This operation was completed with the well-to-seismic-tie tool in OpendTect.

Horizon Tracking

The Heebner shale top, LKC top and LKCD top were tracked for the baseline and M5 surveys. The LKCC top is not uniquely resolved from the LKC and LKCD tops and is not tracked as a result. Because the vibroseis truck lacked a phase-locker, it was necessary to track these horizons manually as they do not exhibit a constant phase throughout the seismic volume. Horizon identification and tracking were further complicated by persistent zones of incoherency, particularly towards the fringes of the surveys. In order to maintain accuracy of horizon picks, tracking was commenced on an inline and crossline transecting the CO2-I #1 well where the synthetic-tie and well logs provide certainty in the picks (Figure 4-5). Tracking was first completed on amplitude cross-sections, snapping to peaks and troughs. In zones of incoherency

no snapping was used and a constant time-depth was used until the reflector was reacquired outside the incoherent zone (Figure 4-4). Once horizons were picked for the entire seismic volume a gridding operation using convex hull triangulation algorithm was used to interpolate the horizon between inlines and crosslines with smoothing to remove jagged edges from the interpolation (Figure 4-6). This workflow produced horizons useful for qualitative interpretation of the data; however, the level of manual input in picking these horizons means that these horizons may diverge from actual seismic response, which is undesirable when studying fluid effects on seismic response at the reservoir level. To solve this issue, the LKC top and LKCD top horizons were tracked again on relative acoustic impedance cross-sections. It was found that relative acoustic impedance data is less sensitive to changes in phase, allowing more use of horizon snapping and allowing seismic response to drive the picks. When picking on relative acoustic impedance data the horizon should be snapped to zero-crossings (Figure 4-7A), which is the equivalent of snapping to peaks/troughs in amplitude data. These relative acoustic impedance horizons were interpolated as before, but with a lesser smoothing operation in order maintain subtle information in the seismic response (Figure 4-7B).

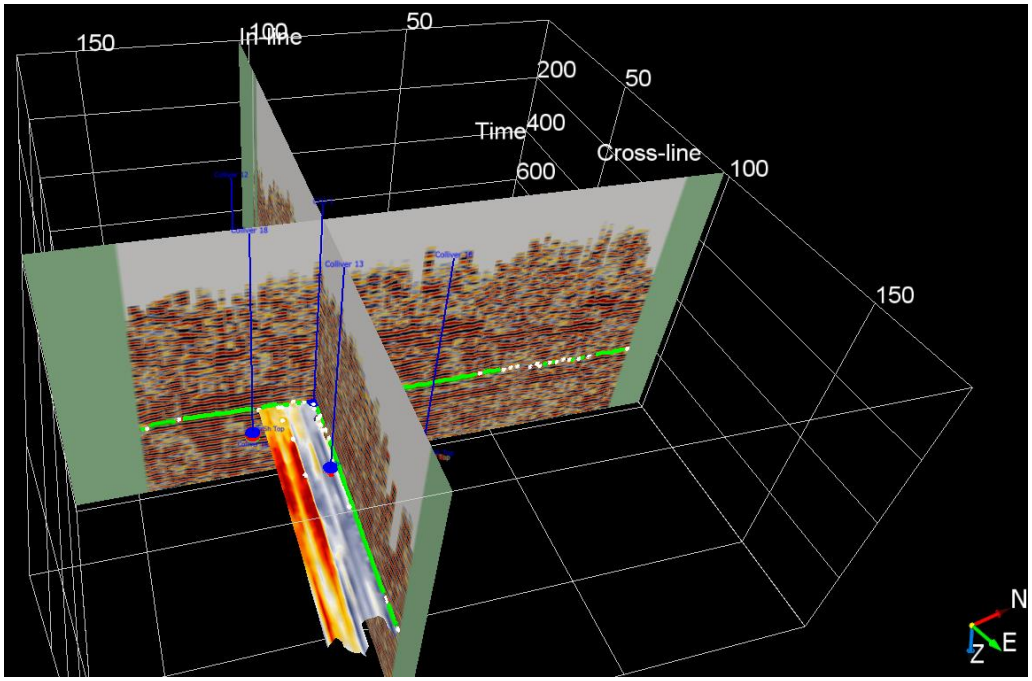

Figure 4-5: Tracking the LKC top horizon in the baseline survey. Tracking was commenced on an inline and crossline transecting the CO2-I #1 well where well control provided certainty in the picks. Note the incoherency of reflectors on the fringes of the survey.

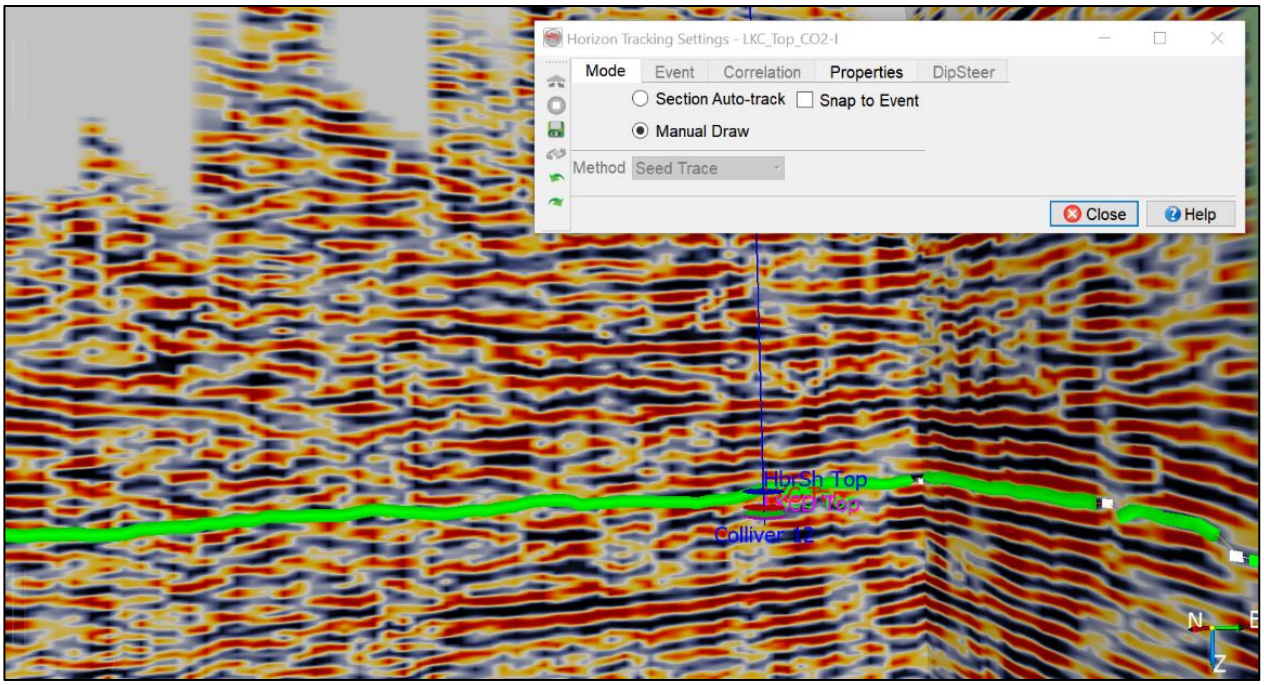

Figure 4-4: Example of manual horizon tracking through a zone of incoherency in amplitude data. The reflectors in the left 3/4 of the image exhibit a high degree of incoherency near the fringe of the survey while the reflectors in the right 1/4 of the image are far more coherent. Manual horizon tracking was completed in OpendTect.

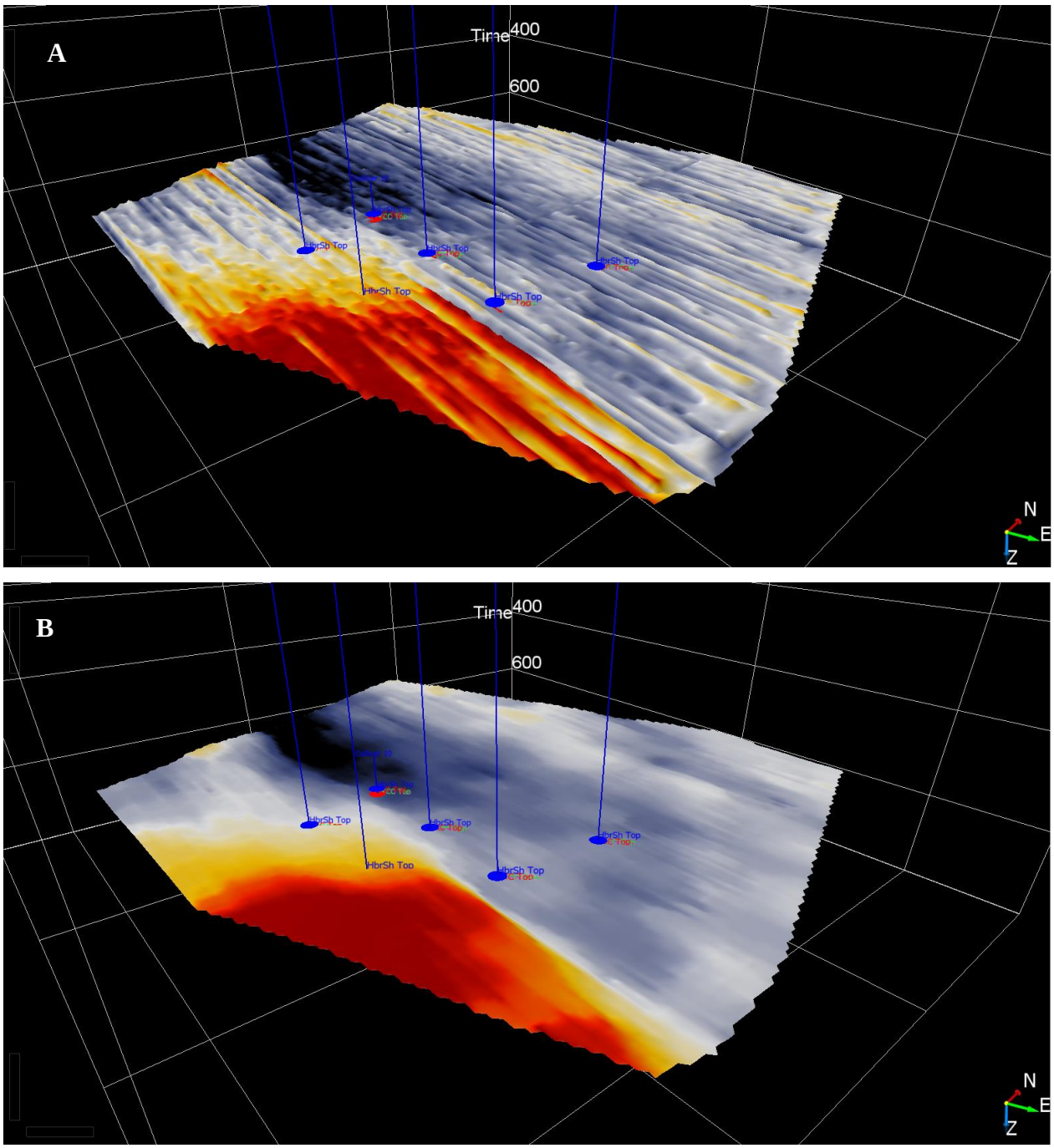

Figure 4-6: (A) BL LKC top after convex hull gridding triagulation operation, and (B) same horizon after applying a median filter with a 5 inline x 5 crossline stepout. This operation was completed with OpendTect.

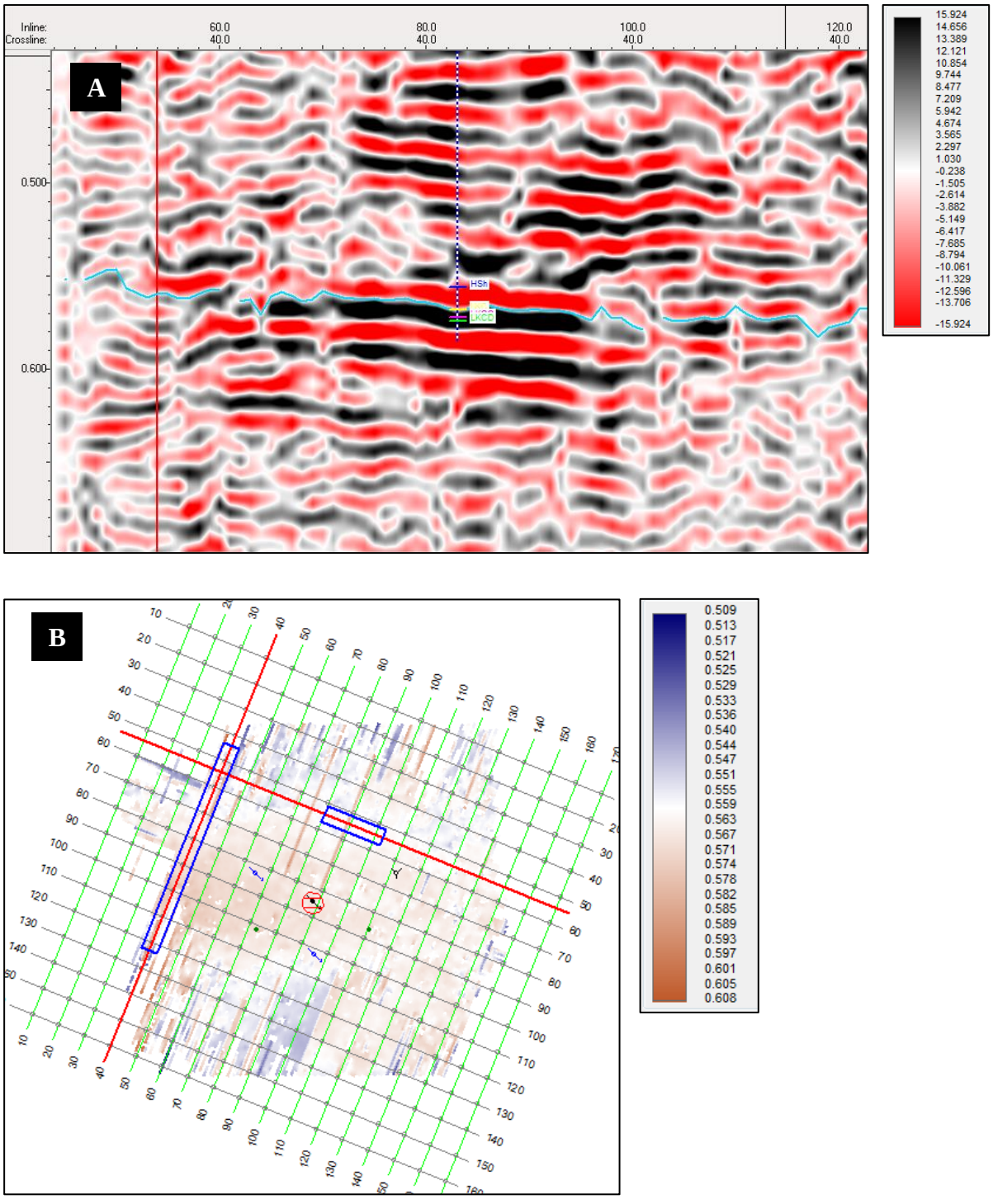

Figure 4-7: (A) Tracking the LKC top horizon on relative acoustic impedance data in the baseline survey, and (B) the BL LKC top horizon in map view. Relative acoustic impedance attribute calculation and tracking were completed in IHS Kingdom.

Tuning Analysis

The simple (two reflector) wedge model in IHS Kingdom was utilized to produce apparent time thickness and normalized amplitude curves (Figure 4-8) for the baseline and fifth monitor surveys utilizing the extracted wavelets from each survey. Isochron maps were created for the BL and M5 surveys utilizing the LKC-Top and LKCD horizons as they fall within the same reflection event and are not uniquely resolved (Figure 4-9). Amplitudes were extracted onto the LKC-Top horizon in OpendTect using stratal amplitudes.

Tuning Correction

A MATLAB script (see Appendix B) was prepared to detune the LKC-Top horizon such that the amplitudes would be dependent solely upon stratigraphic and reservoir fluid inputs on the seismic signal. The script matches isochron values to the apparent time thickness curves and the amplitude values to the normalized amplitude curves displayed in (Figure 4-8). The curves were exported from IHS Kingdom as text files. The isochron maps were exported as ASCII files in the format of X-Y-Isochron values and the amplitude maps were exported as ASCII files in the format of X-Y-Z-Amplitudes with Z values in time. It is important that isochron values be in the same units as the time thickness on the tuning curves (seconds in this case). The script expects input files to be .csv files, necessitating that the text files be converted by opening them in Microsoft Excel and saving them as .csv files.

When run, the script reads in the amplitude, isochron and tuning curve files and stores the values in memory. The isochron values are then interpolated onto the XY grid of the amplitude map in order to account for the possibility that the isochron and amplitude maps were exported with different grids. Isochron values are considered to be apparent time thickness values as they are the result of manual tracking of the observed horizons in the surveys. They are interpolated

onto the apparent time thickness curve in order to obtain the actual time thickness from the wedge model. These actual time thickness values are stored with their corresponding XY values in order to produce a corrected isochron map. The actual time thickness values are then used to find the normalized amplitudes corresponding to these thickness values, which are then used to correct the observed amplitudes using Equation 4-1:

Equation 4-1 : Relationship between horizon amplitude and normalized peak-trough amplitude.

$$A_c = A_H - \frac{1}{2}\left[(\tau_A - 1) * \frac{A_H}{\tau_A}\right]$$

where A_c = amplitude corrected for tuning, A_H = horizon amplitude (amplitude exported with horizon) and τ_A = normalized peak-trough amplitude from the wedge model. The second term is multiplied by a factor of ½ to account for the fact that horizon amplitude is centered on zero while the wedge model utilizes peak-to-trough amplitudes. The corrected isochron and amplitude values are then written to new .csv files that can be converted back to ASCII files.

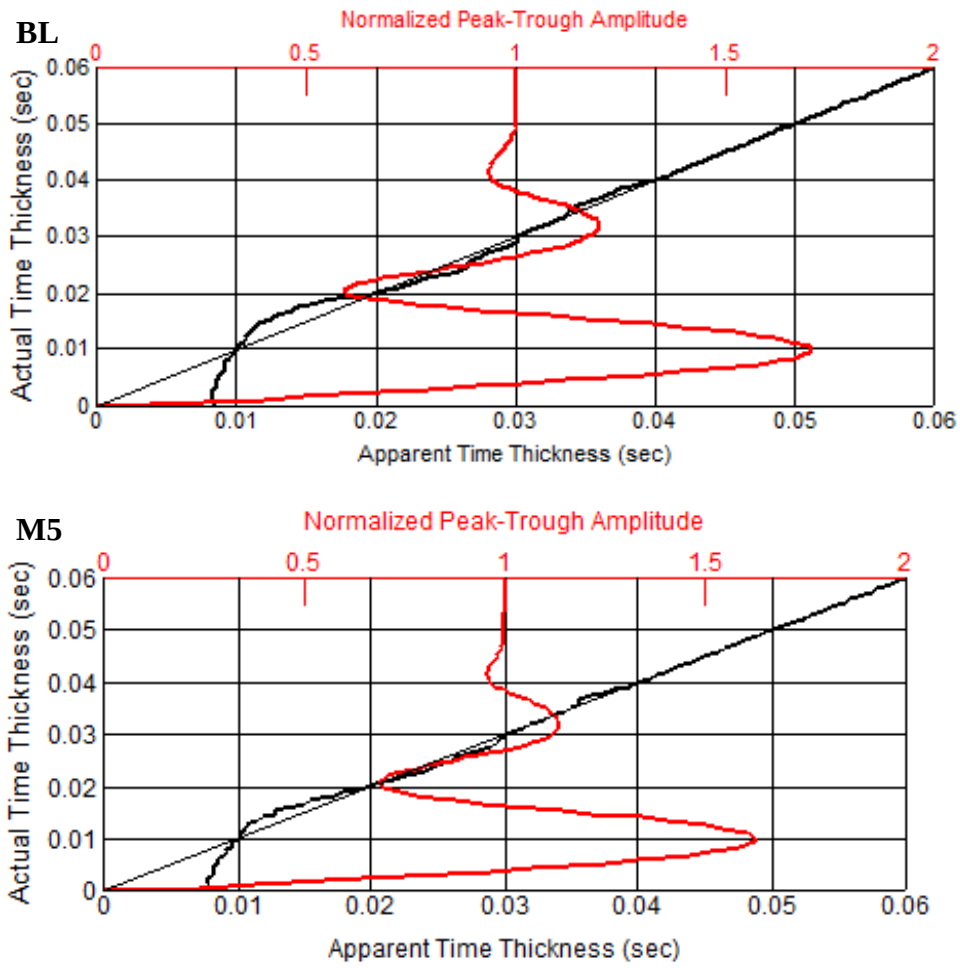

Figure 4-8: Apparent time thickness (black) and normalized amplitude (red) curves for the BL and M5 surveys.

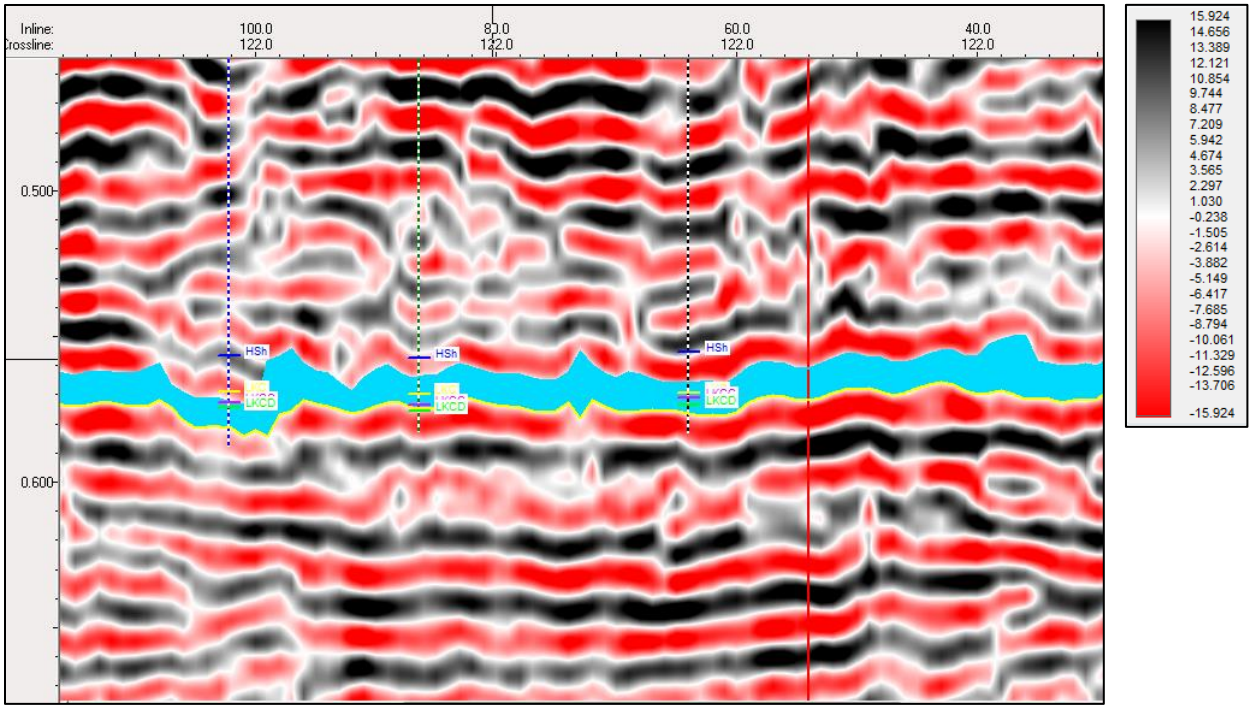

Figure 4-9: Relative acoustic impedance cross-section from the baseline survey. The region highlighted in blue is the isochron used in tuning analysis. Notice that the LKC-Top, LKCC and LKCD zones fall within the same reflection event as the thickness of these horizons is below the resolvable limit of the seismic data. The data is displayed here in IHS Kingdom.

Fluid Replacement Analysis

Fluid replacement analysis was conducted to determine the contribution of supercritical CO_2 saturation of the reservoir to the seismic signal. To achieve this Gassmann's fluid replacement equations are utilized in the form published by Aveseth et al. (2005) (Table 4-2) to determine the change in bulk reservoir density, bulk modulus and P-wave and S-wave velocity. Supercritical CO_2 saturation is assumed to increase at the expense of brine (S_w) (see Appendix C).

Gassmann's Equations

Gassmann's equation entails the following assumptions: (1) the solid rock is homogenous and isotropic, (2) the pores are in communication with one another, (3) wave-induced pressure changes are equilibrated before the onset of the next seismic pulse, and (4) the fluid is frictionless and there is no coupling between the solid and fluid phases (Wang and Nur, 1992). The Plattsburgh limestone is an oomoldic limestone consisting of a calcite matrix with neomorphism in the less permeable layers. Porosities range from 20% - 34.1% and permeabilities range from 1.9 md - 113.9 md (DuBois et al., 2001). In the upper, more permeable zones of the Plattsburgh, the oomolds are intact whilst in the lower, less permeable zone the oomolds exhibit significant fracturing resulting from burial (Figure 2-5). Thus, it may be concluded that the permeable zones of the Plattsburgh satisfy assumption (1) and (2) well. It is generally expected that assumption (3) is satisfied in reflection seismic methods as displacement of rocks at depth resulting from the down-going wave is infinitesimally small. Assumption (4) is expected to be satisfied by the tendency of supercritical CO_2 to lower the viscosity of reservoir fluids that it enters solution with.

Table 4-2: Gassmann's fluid replacement equations in the form published by Aveseth et al. (2005).

Equations
$\rho_{f_b} = \sum_i \rho_{f_i} S_{f_i}$
$\rho_{b1} = \rho_{f_b} + \rho_{mineral}(1-\phi)$
$K_{sat1} = \rho_{b1}\left(V_{p1}^2 - \frac{4}{3}V_{s1}^2\right)$
$K_{f1} = \left(\frac{1-s_w}{K_{oil}} + \frac{S_w}{K_{brine}}\right)^{-1}$

$$K_{f2} = \left(\frac{1-(S_w - S_{CO_2}}{K_{oil}} + \frac{S_w - S_{CO_2}}{K_{brine}} + \frac{S_{CO_2}}{K_{CO_2}}\right)^{-1}$$
$$\mu_{sat1} = \rho_{b1}(V_{s1}^2) = \mu_{sat2}$$
$$\rho_{b2} = \rho_{b1} + \phi\left(\rho_{f2} - \rho_{f1}\right)$$
$$K_{sat2} = \frac{K_{mineral}}{\left[\frac{K_{sat1}}{K_{mineral}-K_{sat1}} - \frac{K_{f1}}{\phi\left(K_{mineral}-K_{f1}\right)} + \frac{K_{f2}}{\phi(K_{mineral}-K_{f2}}\right]^{-1} + 1}$$
$$V_{p2} = \sqrt{\frac{K_{sat2} + \frac{4}{3}\mu_{sat2}}{\rho_{b2}}}$$
$$V_{s2} = \sqrt{\frac{\mu_{sat2}}{\rho_{b2}}}$$

Table 4-3: Gassmann equation variables and definitions.

Variable	Definition
ρ_{f_b}	Bulk fluid density (g/cc)
ρ_{f_i}	Component fluid density (g/cc)
S_{f_i}	Component fluid saturation (percent expressed as a decimal)
ρ_b	Bulk reservoir density (g/cc)
$\rho_{mineral}$	Rock frame density (g/cc)
ϕ	Porosity (percent expressed as a decimal)
K_{sat1}	Initial reservoir bulk modulus (GPa)
ρ_{b1}	Initial reservoir bulk density (g/cc)
V_{p1}	Initial P-wave velocity (m/s)

V_{s1}	Initial S-wave velocity (m/s)
μ_{sat1}	Initial reservoir shear modulus (GPa)
μ_{sat2}	Reservoir shear modulus after fluid replacement (GPa)
ρ_{f2}	Bulk fluid density after fluid replacement (g/cc)
ρ_{b2}	Bulk reservoir density after fluid replacement (g/cc)
K_{sat2}	Reservoir bulk modulus after fluid replacement (GPa)
$K_{mineral}$	Rock frame bulk modulus (Gpa)
K_{f1}	Initial fluid bulk modulus (Gpa)
K_{f2}	Fluid bulk modulus after fluid replacement (GPa)
V_{p2}	P-wave velocity after fluid replacement (m/s)
V_{s2}	S-wave velocity after fluid replacement (m/s)

Table 4-4: Initial values used in Gassmann's fluid replacement analysis.

Variable	Initial Value	Source
K_1	60.83761564 (GPa)	Obtained from ultrasonic velocity measurements on rock cores
K_{brine}	2.340000 (GPa)	Mougin et al. (2002)
K_{oil}	2.350000 (GPa)	Median value from several online sources (to be refined if lab data becomes available)
K_{CO_2}	0.382120 (GPa)	CO_2 properties table
ϕ	0.30 (percent expressed as a decimal)	DuBois et al. (2001)

$\rho_{mineral}$	2.73 (g/cc)	Obtained from ultrasonic velocity measurements on rock cores
ρ_{b1}	2.357268293 (g/cc)	Obtained from the reservoir interval of the high-resolution formation density log at the CO2-I #1 well
ρ_{brine}	1.050 (g/cc)	Obtained from KGS Brine Database for lower Pennsylvanian brine in Russell county
ρ_{oil}	0.834 (g/cc)	Byrnes (2011)
ρ_{co_2}	0.96750 (g/cc)	CO_2 properties table
σ_{rock}	0.4018 (GPa)	Poisson's ratio obtained from ultrasonic velocity measurements on rock cores from the CO2-I #1 well
V_{p1}	4622.390613 (m/s)	Calculated from the reservoir interval of the sonic log at the CO2-I #1 well
V_{s1}	1872.833556 (m/s)	Calculated from the reservoir interval of the sonic log at the CO2-I #1 well using the relationship between Poisson's ratio, V_p and V_s outlined in Equation 4-2
S_w	0.70	Used as a starting point, should be refined using production data. S_w cannot be calculated using Archie's

		equation because reservoir has undergone extensive production and waterflooding prior to CO_2 enhanced oil recovery program

Ultrasonic Velocity Measurements

In order to overcome the lack of available shear-wave data, samples were obtained for the upper, middle and lower portions of the Plattsburgh limestone from the Kansas Geological Survey Kansas Core Library for the CO2-I #1 well. As these cores have been the subject of several past studies, limited material was available for ultrasonic velocity measurements. However, two samples of sufficient size to fit in the hydraulic press located in Dr. Raef's lab were obtained, albeit not for the porous interval of the reservoir; a cylindrical core from 2891 ft depth and a half cylinder from 2913 ft depth (Figure 4-10). However, as both cores exhibit primarily a limestone composition similar to the porous interval, they are sufficient for obtaining a relationship for P-wave and S-wave velocity. This relationship is dependent upon Poisson's ratio (σ) in the following manner:

Equation 4-2: Relationship between Poisson's ratio, V_p and V_s.

$$V_s = \sqrt{\frac{V_p^2\left(\frac{1}{2} - \sigma\right)}{1 - \sigma}}$$

Poisson's ratio was determined experimentally by measuring ultrasonic P-wave and S-wave velocities in the core samples. The following procedure was adhered to in these experiments:

The mass, volume and length of the cores were recorded. The volume was measured using the water displacement method (Figure 4-12) after the cores are weighed so as to avoid including the mass of the water in the measurement. The cores were then placed into the

hydraulic press with an ultrasonic wave transmitter located on one end of the core and a receiver located on the other end of the core (Figure 4-11). A thin film of honey was spread over contacts of the core sample and transmitter/receiver in order to couple the core sample to the transmitter/receiver. When the test begins, ultrasonic waves are imparted into the core by the transmitter. At this exact moment the receiver starts to record the signal. The lag time between the start of the experiment and the time when waves are first recorded by the receiver is used to determine the velocity of the wave through the core sample. This was done for increasing pressure increments of 500 pounds starting at 2000 pounds up to the point of failure for both cores. The 2891 ft core maxed out at 5000 pounds while the 2913 ft core maxed out at 7500 pounds. First arrival times of the P-wave and S-wave were determined for each of these pressure steps (Figure 4-13 and Figure 4-14) allowing Poisson's ratio to be found for each. From these experiments an average Poisson's ratio of $\sigma = 0.4018$ was found for the reservoir.

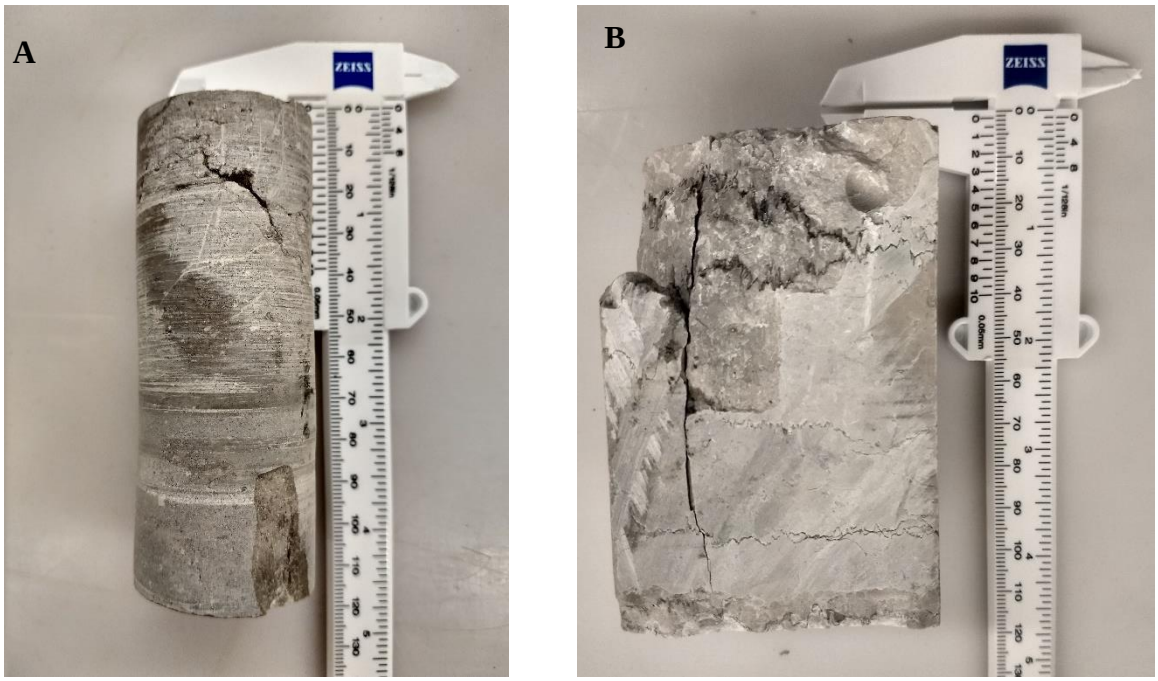

Figure 4-10: (A) 2891 ft cylindrical core sample, and (B) 2913 ft half cylinder core sample. Both core samples were obtained from the CO2-I #1 well. Note that these images were acquired after testing and that the fractures are a result of failure during the test.

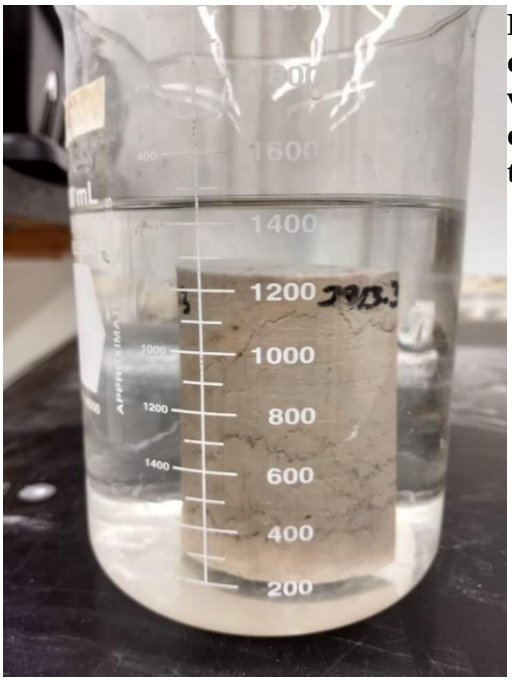

Figure 4-12: Measuring the volume of the 2913 ft core with the water displacement method. A known volume of water is added to the beaker and the change in volume when the sample is added is used to measure the volume of the sample.

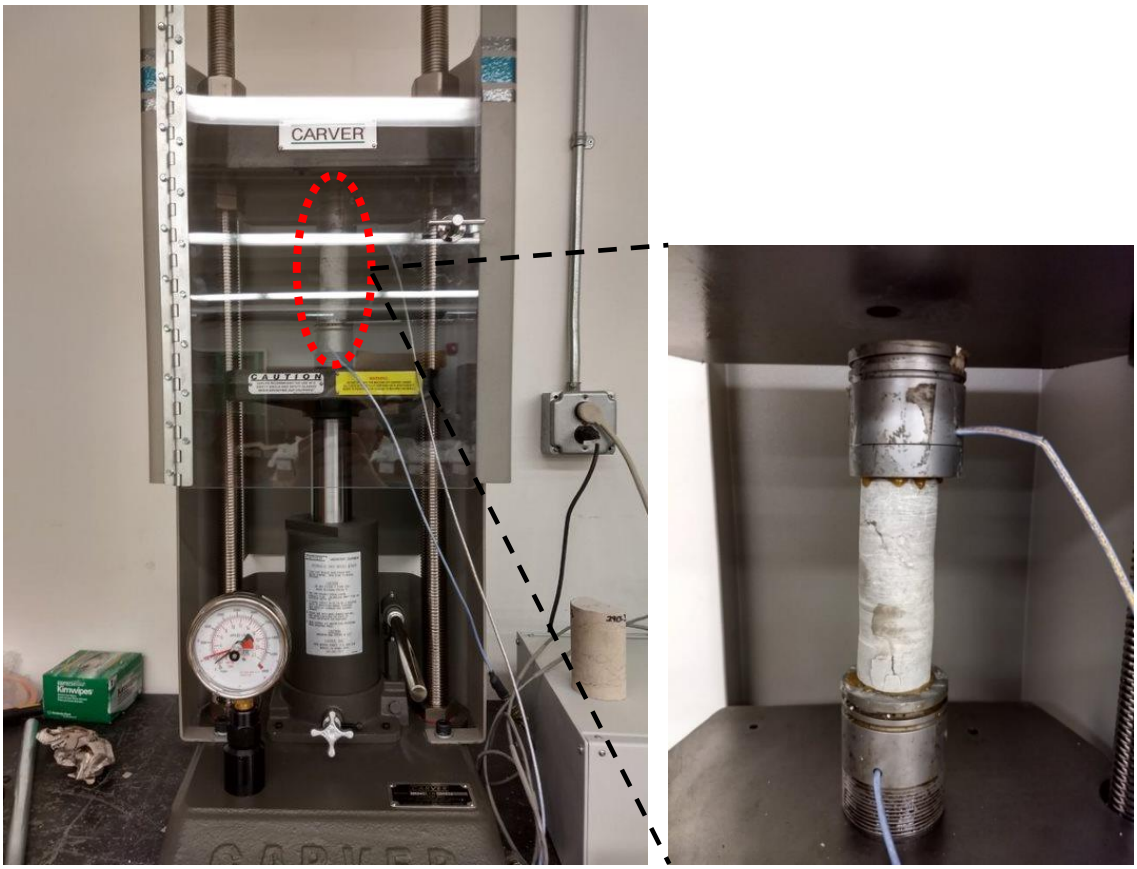

Figure 4-11: Core samples are placed in a hydraulic press between an ultrasonic transmitter and receiver. A thin film of honey is spread between the sample and the transmitter and receiver to ensure proper coupling. The transmitter and receiver are wired to a GCTS Testing Systems ULT-100 Ultrasonic interface, which is driven by the GCTS C.A.T.S. Ultrasonics software installed on the desktop computer located in Dr. Raef's lab.

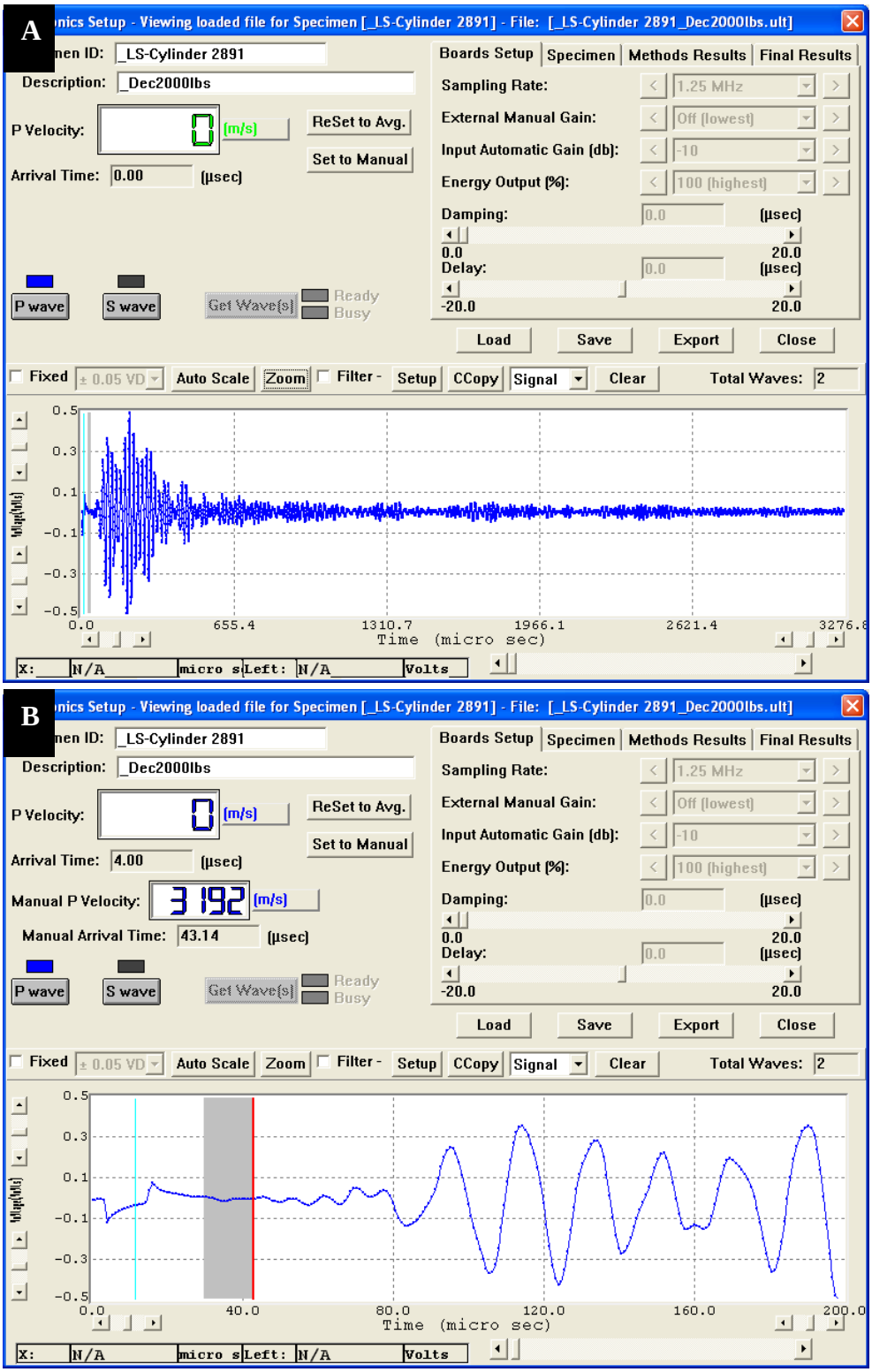

Figure 4-13: (A) Overview of the P-wave signal for the 2891 ft core after one of the tests, and (B) picking of the P-wave first arrival time. The initial oscillation in the signal is noise that is repeated in every test. It is the result of a spike in voltage when the sensor is turned on. The first arrival of the P-wave is located at the red vertical line, after the startup noise has attenuated. The software used is GCTS C.A.T.S. Ultrasonics.

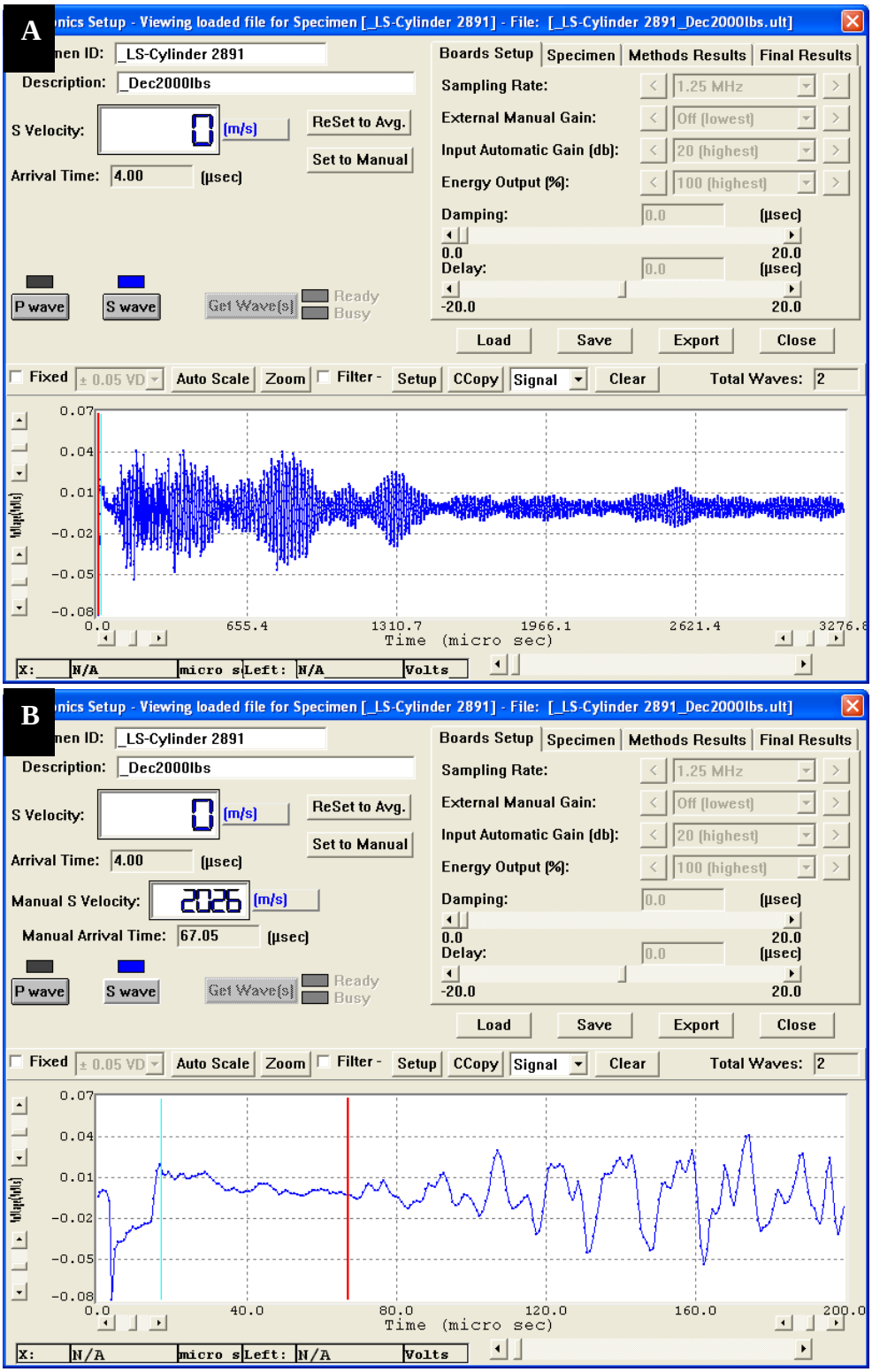

Figure 4-14: (A) Overview of the S-wave signal for the 2891 ft core after one of the tests, and (B) picking of the S-wave first arrival time. The initial oscillation in the signal is noise that is repeated in every test. It is the result of a spike in voltage when the sensor is activated. The first arrival of the S-wave is located at the red vertical line, after the startup noise has attenuated. The software used is GCTS C.A.T.S. Ultrasonics.

Chapter 5 - Results

De-Tuned Seismic

The isochron maps of the baseline (Figure 5-1) and M5 (Figure 5-3) surveys were de-tuned according to modeled seismic response using extracted wavelets and observed time thickness values of the isochron maps. Both corrected isochron maps exhibit increased textural variation, suggesting that tuning was masking the more subtle seismic response to conditions at the reservoir level. Amplitude horizons for the baseline and M5 surveys were also corrected for tuning, matching the amplitude values to the normalized peak-trough curve (Figure 4-8) and applying the correction in Equation 4-1. Areas of very high amplitude, which appear as bright yellow on the amplitude maps, were observed after applying the correction, particularly in the M5 survey. These correspond to areas where the isochron thickness nears zero and should be removed before the horizons are used for interpretation. Areas where the isochron thickness nears zero and where there are holes in the isochron maps are the result of zones of incoherency where data is sparse or the result of the LKC-LKCD reflector changing phase, causing the LKC top and LKCD horizons to cross and create negative isochron values which were filtered out by the tuning correction script. Anomalous isochron thicknesses (i.e., very high or very low isochron values) are observed at the edges of the baseline and M5 surveys, which correspond to zones of high incoherency (Figure 4-4). As a result, interpretations will exclude the fringes of the surveys and be limited to the region bound by the box in Figure 5-1, Figure 5-2, Figure 5-3 and Figure 5-4.

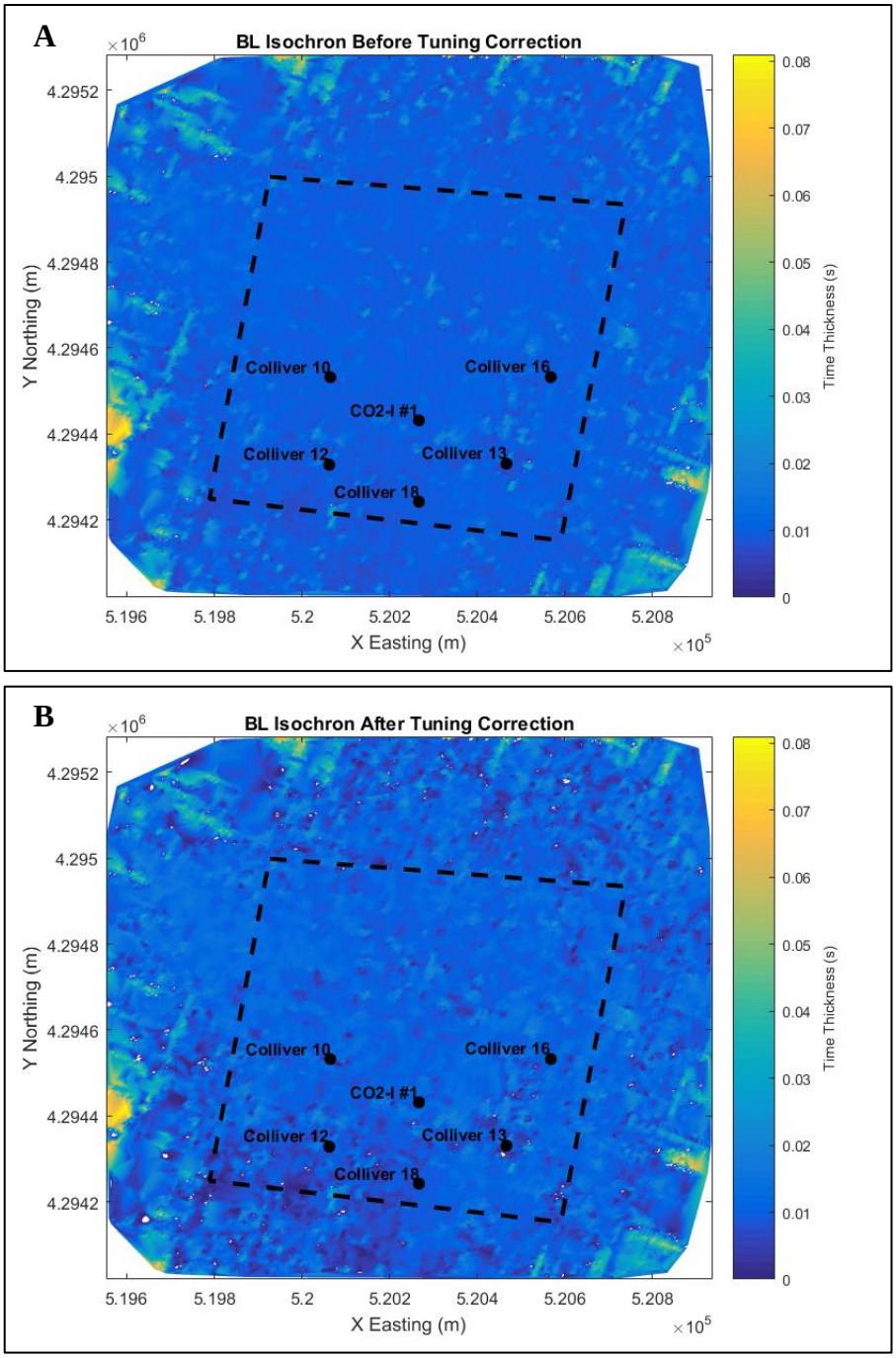

Figure 5-1: (A) Baseline LKC-LKCD top Isochron maps before and (B) after tuning correction. Values were interpolated to the apparent time thickness curve. Holes represent areas where the data is sparse due to zones of incoherency.

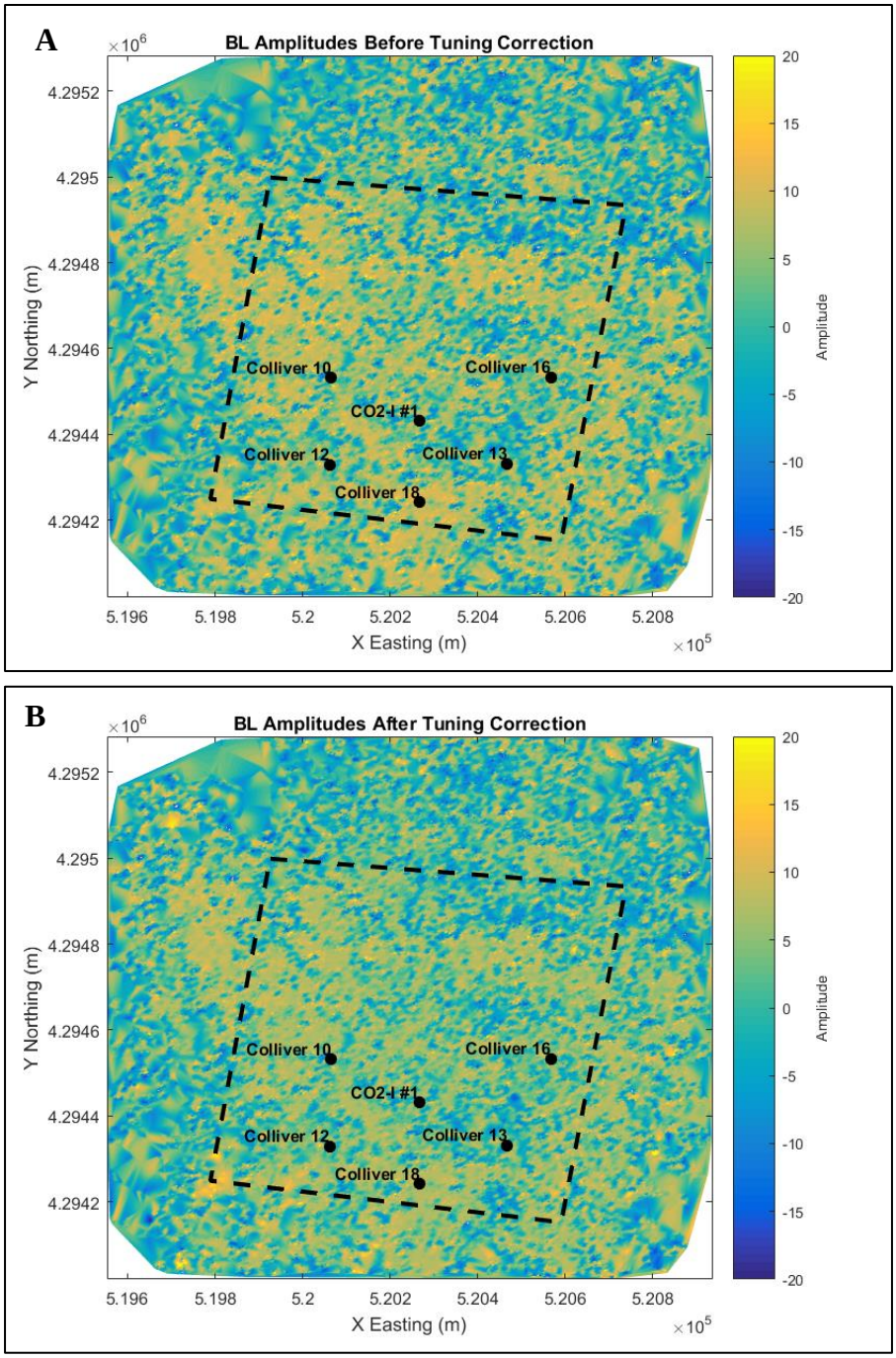

Figure 5-2: (A) Baseline Amplitude maps before and (B) after tuning correction. Values were interpolated to normalized amplitude curve.

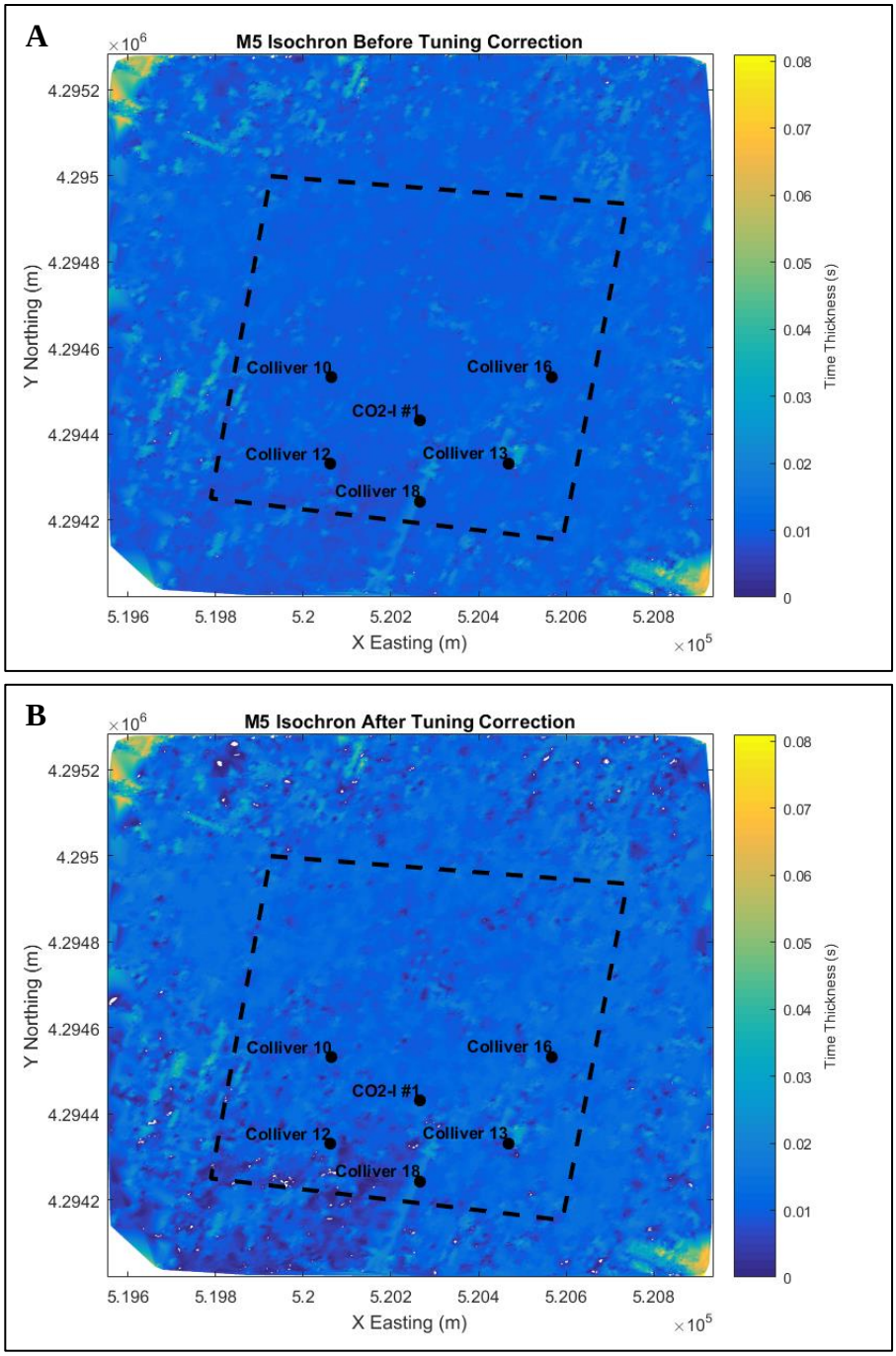

Figure 5-3: (A) M5 LKC-LKCD top Isochron maps before and (B) after tuning correction. Values were interpolated to the apparent time thickness curve. Holes represent areas where the data is sparse due to zones of incoherency.

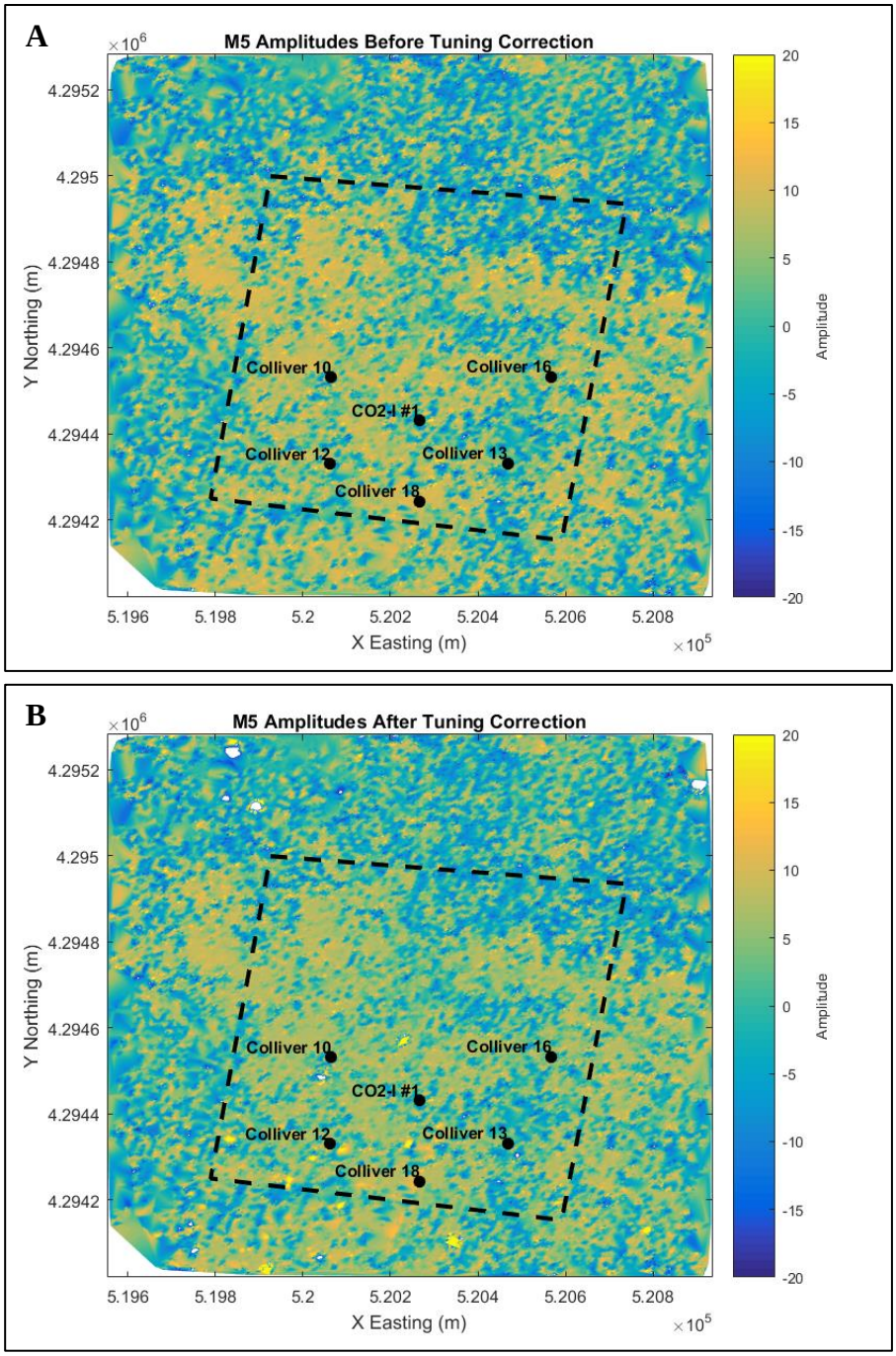

Figure 5-4: (A) M5 Amplitude maps before and (B) after tuning correction. Values were interpolated to normalized amplitude curve.

Fluid Replacement Analysis

Fluid replacement modeling was conducted to predict the change in seismic response due to supercritical CO_2 saturation of the reservoir utilizing Gassmann's equations as given in Table 4-2 with the input parameters given in Table 4-4. Supercritical CO_2 saturation was assumed to increase at the expense of brine such that for a starting S_w of 70%, the maximum S_{CO_2} possible will be 70%. Bulk reservoir properties were calculated for every 10% increase in supercritical CO_2 saturation to produce plots for bulk reservoir density (Figure 5-5), bulk modulus (Figure 5-6), P-wave velocity (Figure 5-7) and seismic impedance (Figure 5-8) against supercritical CO_2 saturation.

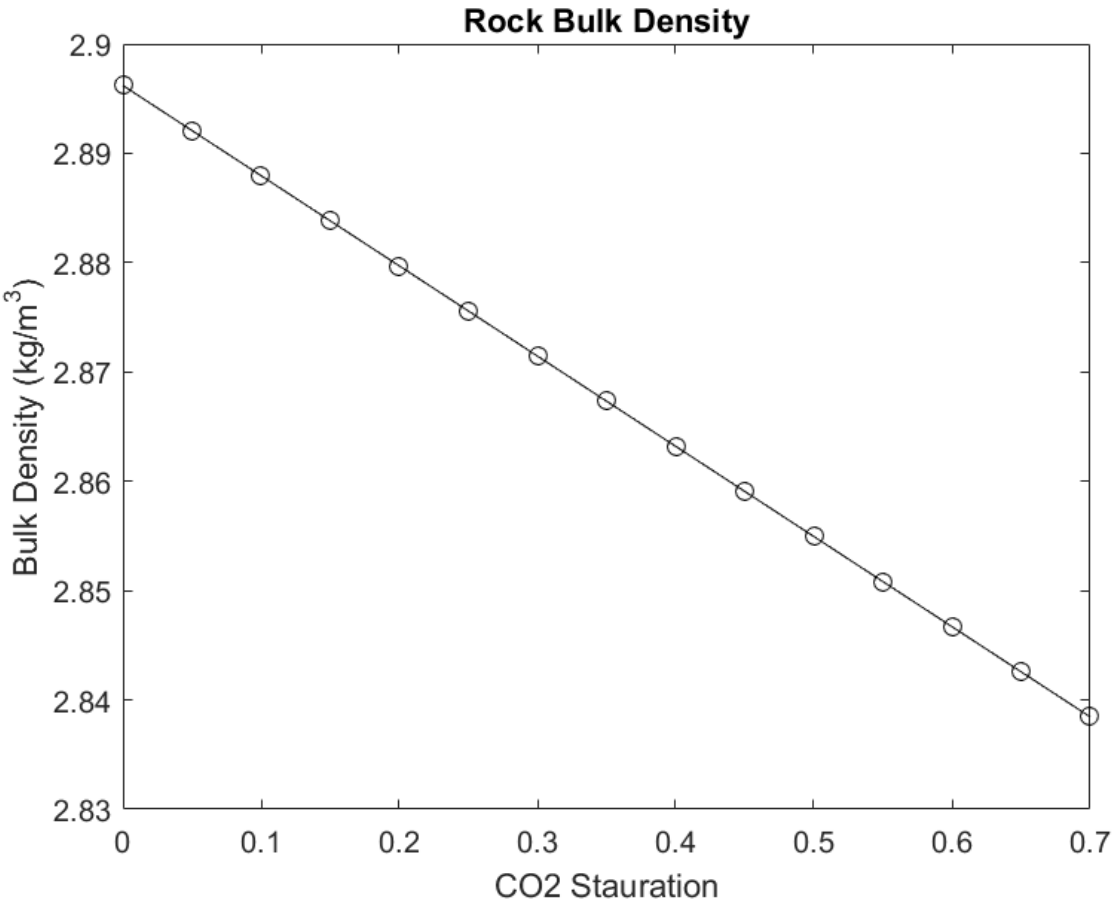

Figure 5-5: Bulk reservoir density as a function of supercritical CO_2 saturation.

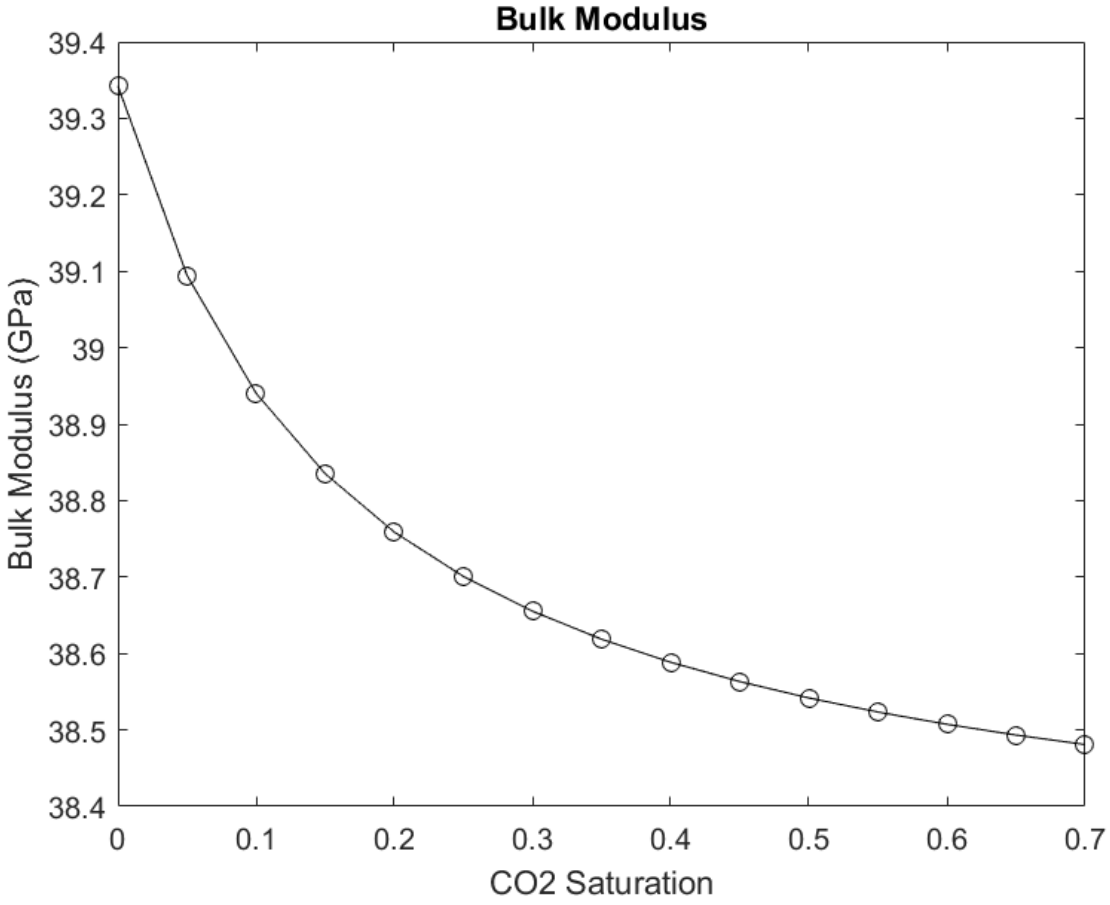

Figure 5-6: Bulk modulus as a function of supercritical CO_2 saturation. Bulk modulus declines sharply until $S_{CO_2} = 0.2$ and then continues to decline at a decreasing rate. In practice, reservoir pressure will also affect the shape of this curve and may cause it to level off at a lower supercritical CO_2 saturation.

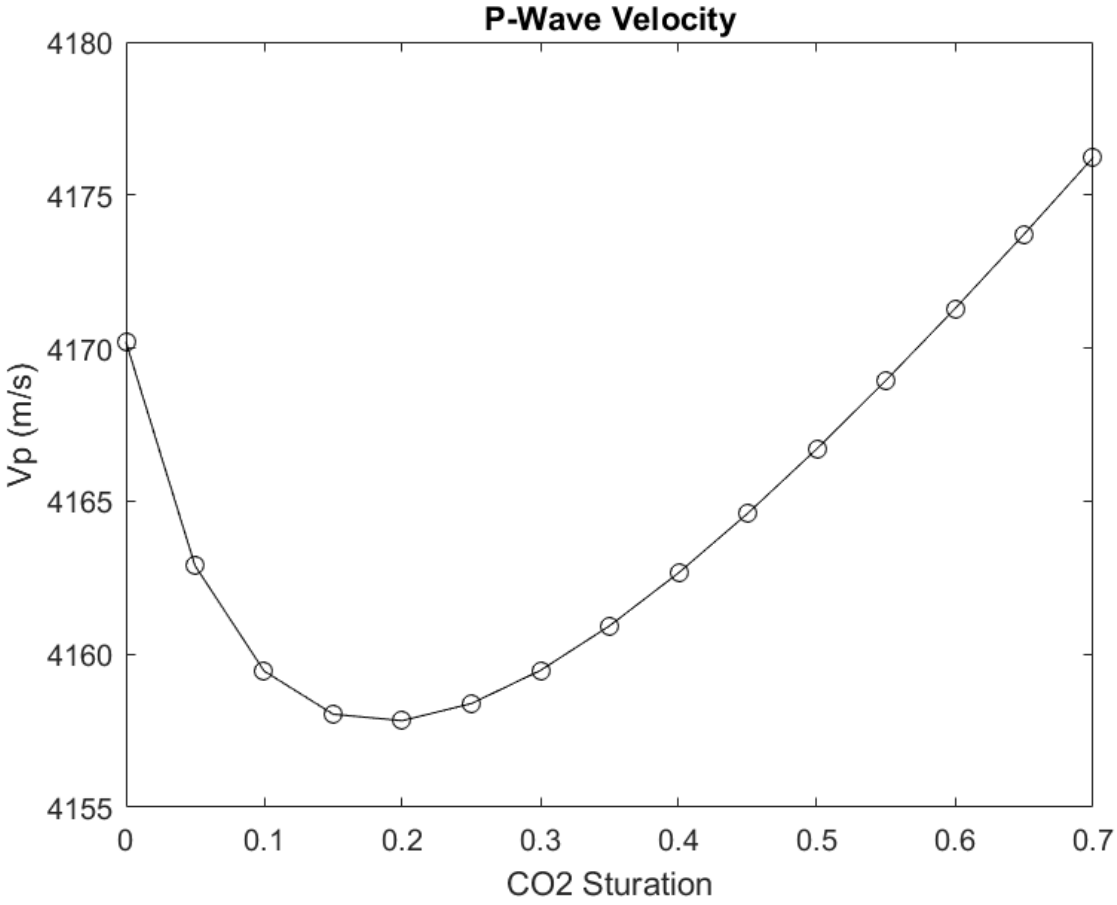

Figure 5-7: P-wave velocity as a function of supercritical CO_2 saturation. An initial sharp decline in bulk modulus results in a rapid decrease in P-wave velocity up to $S_{CO_2} = 0.2$ when the effect of a decreasing bulk density (in the denominator, see Table 4-2) causes the P-wave velocity to increase. In practice, reservoir pressure will also affect the shape of this curve and P-wave velocity will not increase indefinitely, as it is limited by CO_2 saturation.

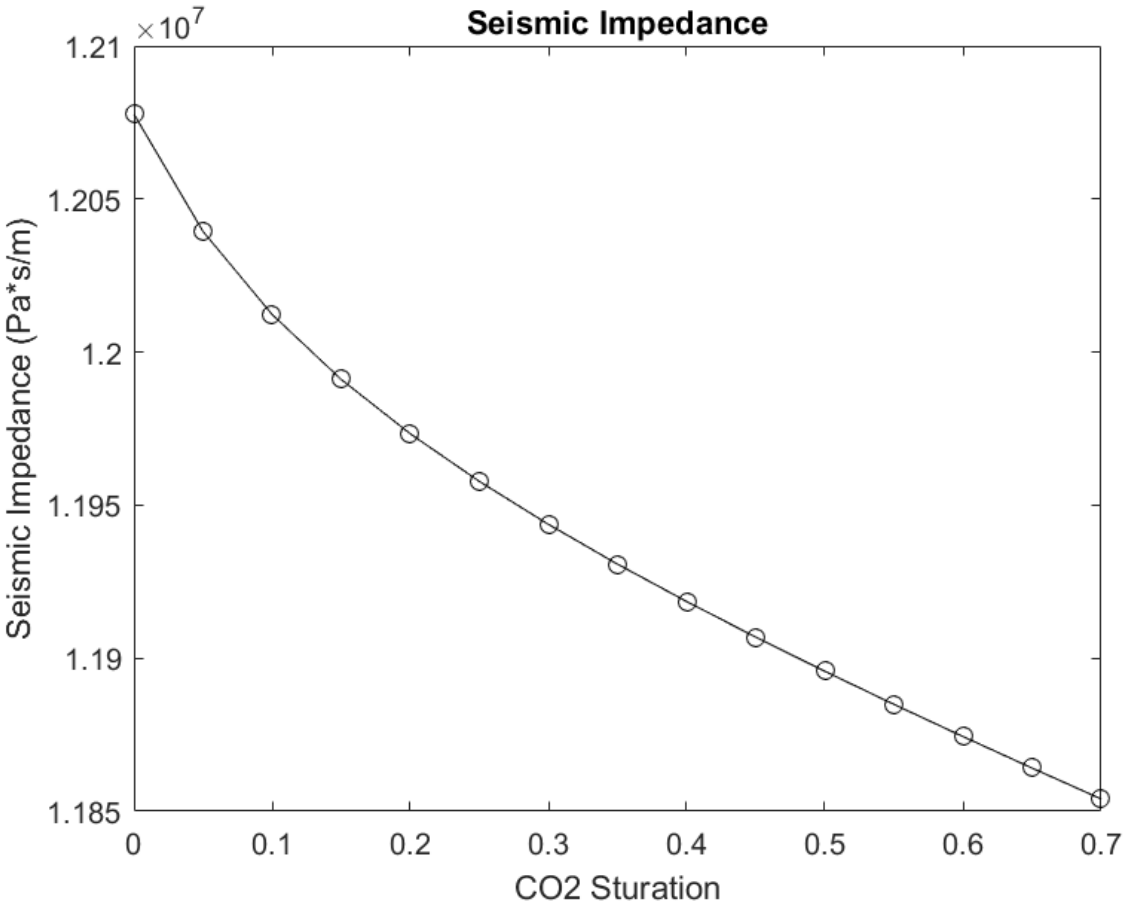

Figure 5-8: Seismic impedance as a function of supercritical CO_2 saturation.

Chapter 6 - Discussion

Analysis

Tuning Correction

Histograms of the LKC top – LKCD top isochron values for the baseline and M5 surveys both exhibit distributions centered on 8-13 ms, the centers of which were shifted to larger time thickness values after applying the tuning correction (Figure 6-1 and Figure 6-2). This suggests that reflectors with time thickness values of 8-13 ms were most heavily impacted by tuning in these surveys. This is supported by the clustering of points around 11 ms in the amplitude vs isochron plots of the baseline and M5 surveys (Figure 6-3). Amplitude vs time thickness plots are useful for indicating whether tuning is present in the data, as there should be no correlation between time thickness and amplitude for data unaffected by tuning. In the LKC top – LKCD top isochron horizons of the baseline and M5 surveys, points with isochron thicknesses in the range of 8-13 ms exhibit a consistent brightening or increase in the magnitude of amplitudes when compared with other points in the LKC top – LKCD top isochron horizons. It can be observed that after the tuning correction is applied the magnitudes of the amplitudes for these points are decreased and the correlation between amplitude and time thickness is removed, indicating that the tuning correction has achieved the desired result of removing the effect of tuning from amplitude. Histograms of amplitude magnitudes before and after applying the tuning correction in the baseline and M5 surveys also exhibit a general dimming or decrease in the magnitudes of amplitudes after applying the tuning correction, which can also be observed in the amplitude maps of the baseline and M5 surveys (Figure 5-2 and Figure 5-4).

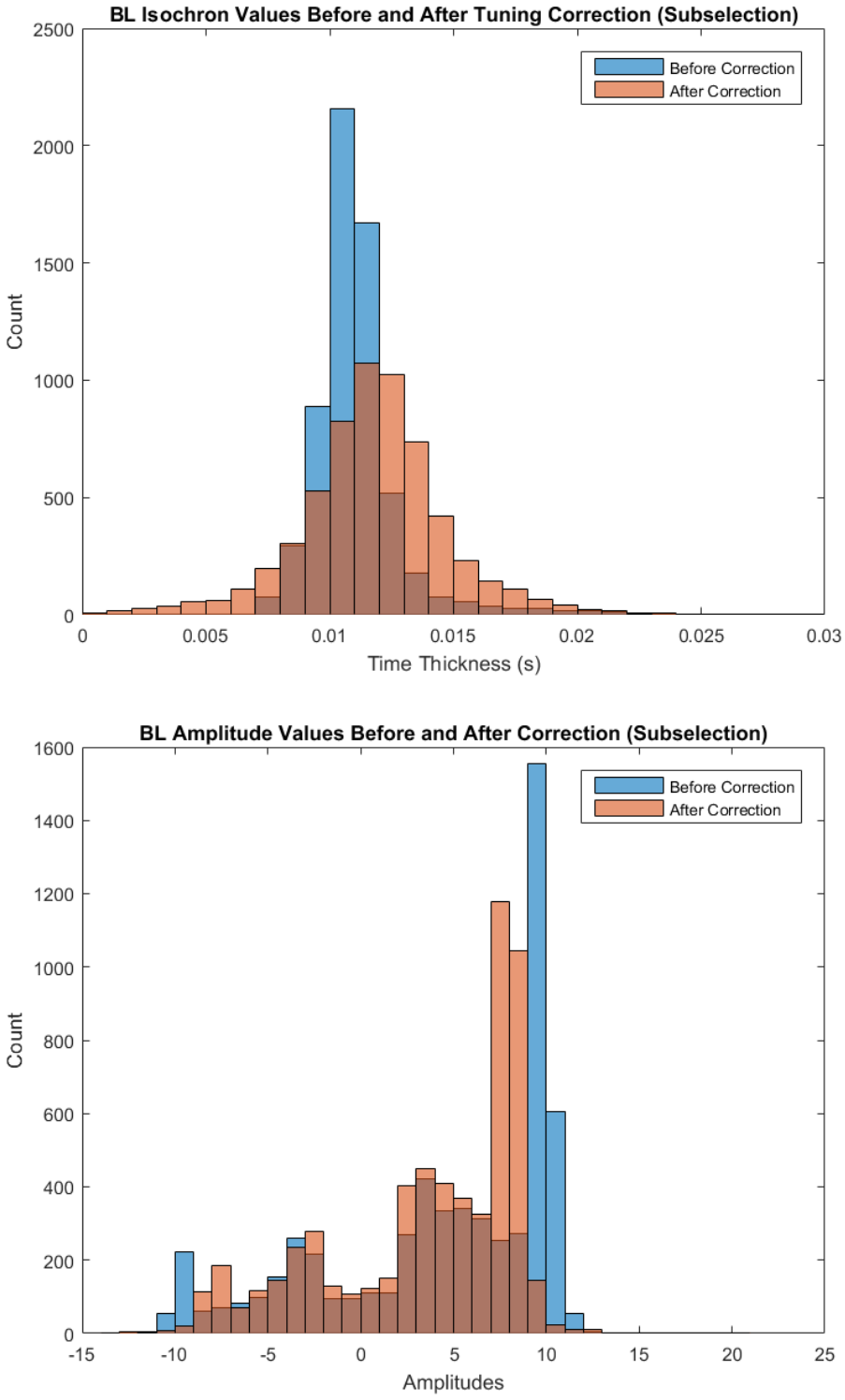

Figure 6-1: Overlain histograms of baseline survey isochron and amplitude values before and after applying the tuning correction in the region enclosed by the box (Figure 5-1 and Figure 5-2). Portions where the orange histogram is darker indicate where it overlies the blue histogram behind it.

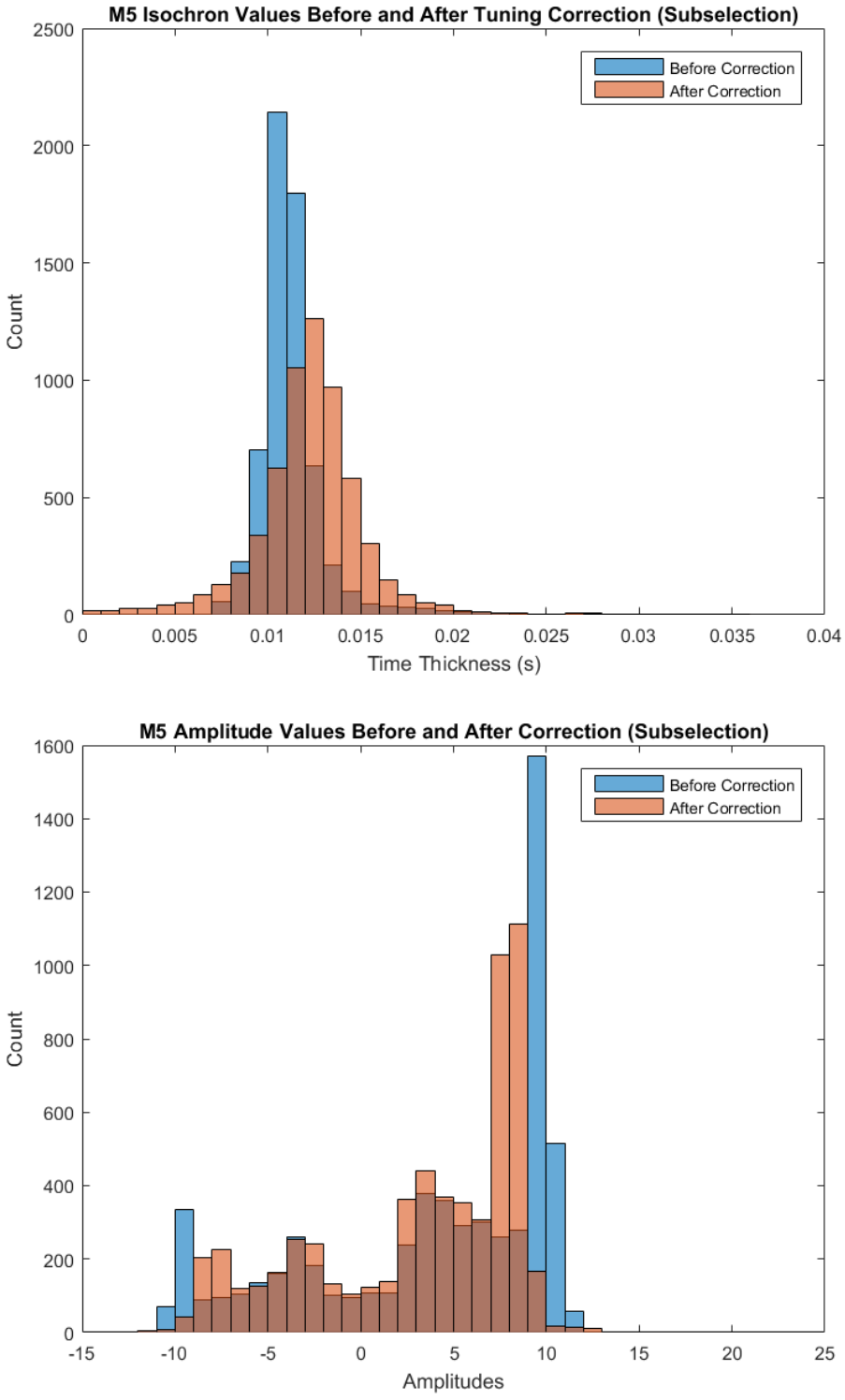

Figure 6-2: Overlain histograms of M5 survey isochron and amplitude values before and after applying the tuning correction in the region enclosed by the box (Figure 5-3 and Figure 5-4). Portions where the orange histogram is darker indicate where it overlies the blue histogram behind it.

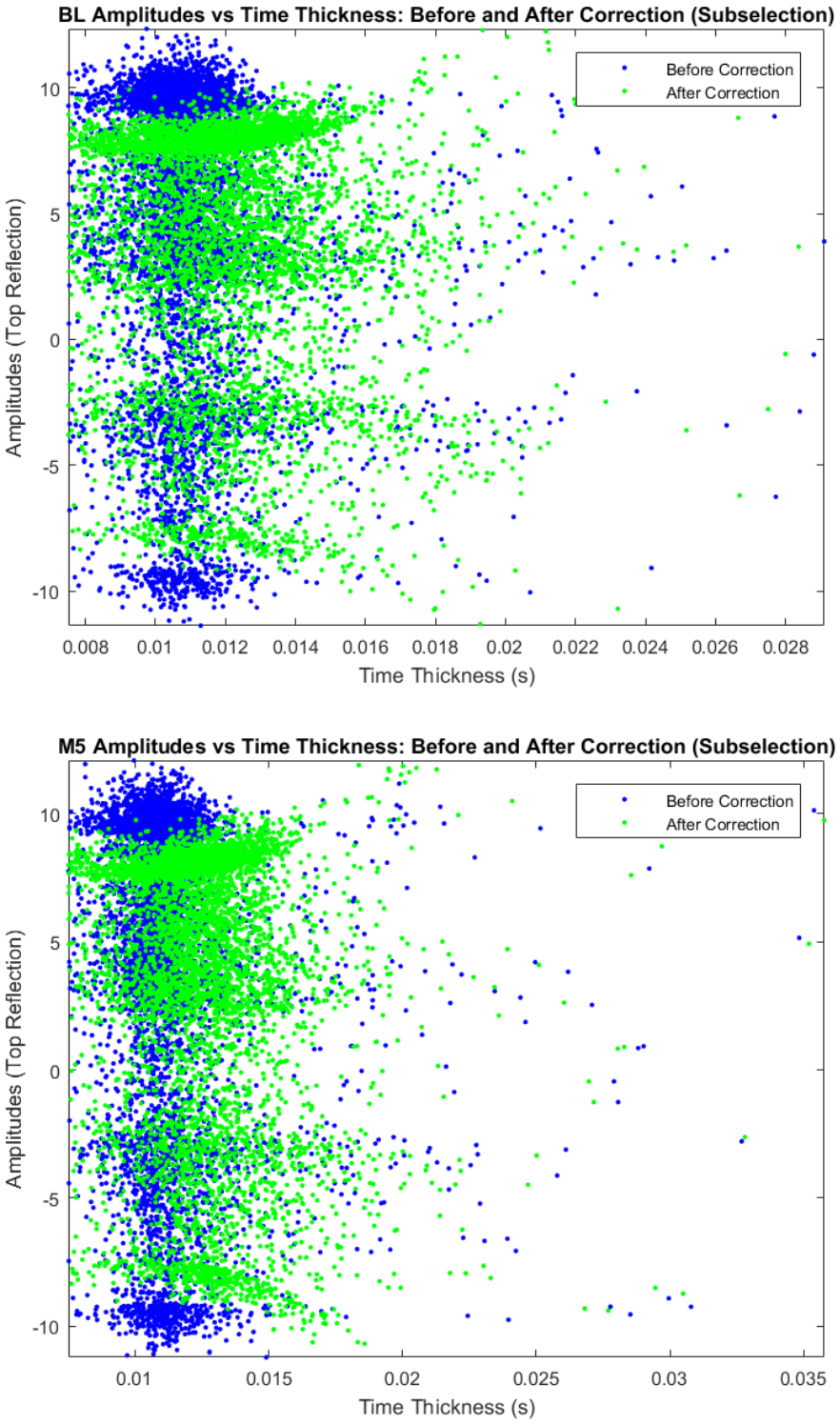

Figure 6-3: Baseline and M5 survey amplitudes vs isochron thickness plots. The clustering of the uncorrected points (blue) around 8-13 ms is an indication that data in the time thickness range is affected by tuning. After applying the tuning correction (green points) this geometry is no longer present.

Fluid Replacement Modeling

The predicted change in bulk reservoir properties due to supercritical CO_2 injection up to $S_{CO_2} = 0.7$ and $S_{oil} = 0.3$ yielded a 2% decrease in bulk reservoir density, a 1.85% decrease in seismic impedance and a maximum change in P-wave velocity of 0.30% at $S_{CO_2} = 0.2$ (Figure 6-4). When taking these changes into account, the maximum change in amplitude can be predicted using Equation 6-1 to calculate the reflection coefficient of the interface between two seismic reflectors:

Equation 6-1: Reflection coefficient between two seismic reflectors.

$$\frac{\rho_1 V_1 - \rho_2 V_2}{\rho_1 V_1 + \rho_2 V_2}$$

where $\rho_1 = 2.48$ g/cc and $V_1 = 3828.077$ m/s for the Heebner shale, and $\rho_2 = 2.90$ g/cc and $V_2 = 4170$ m/s for the LKC top – LKCD top interval. The Heebner shale density and interval velocity were obtained by averaging the Heebner shale interval of the high-resolution formation density log and sonic log inverted to obtain P-wave velocities at the CO2-I #1 well, while the values for the LKC top – LKCD top interval were obtained through the ultrasonic velocity measurements on the core samples from the CO2-I #1 well. This yields an initial reflection coefficient (RC) of $RC = -0.120$. Calculating the reflection coefficient again using the bulk reservoir density $\rho_2' = 2.84$ g/cc and P-wave velocity $V_2' = 4176$ m/s predicted in fluid replacement modeling after supercritical CO_2 saturation of the reservoir, a new reflection coefficient of $RC = -0.110$ is obtained. This represents an ~8% change in reflection coefficient after supercritical CO_2 saturation of the reservoir, which would correspond to an equivalent change in seismic amplitude at the LKC – Heebner shale interface. Horizon amplitude difference maps displaying the change in horizon amplitude between the M5 and baseline surveys

($M5_{amplitudes} - BL_{amplitudes}$), depict a widespread change in LKC top horizon amplitudes, with no distinct injection related change limited to the vicinity of the CO2-I #1 well (Figure 6-5).

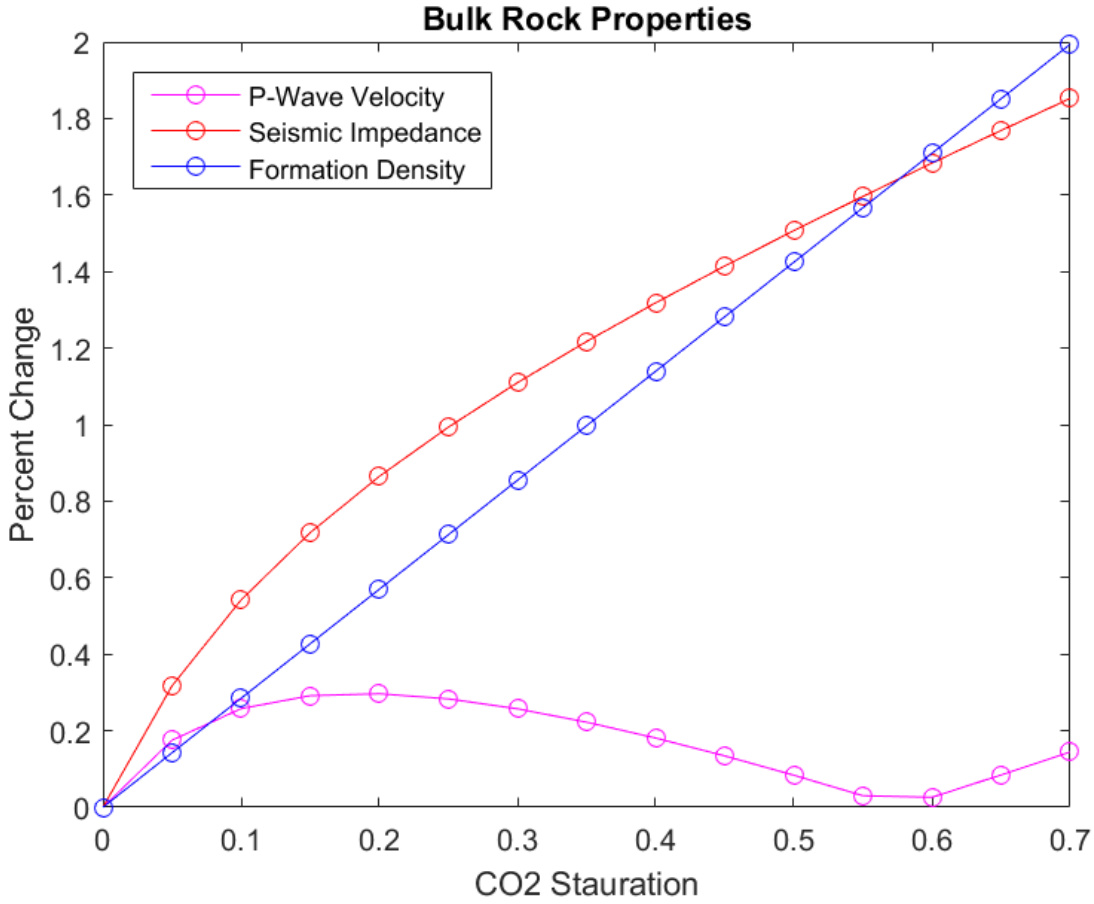

Figure 6-4: Percent change of bulk rock properties from fluid replacement modeling for a reservoir with the following properties: $\phi = 30\%$, $S_w = 0.70$, $S_{oil} = 0.30$. Supercritical CO_2 saturation is allowed to increase at the expense of brine. For the bulk change in these values see Figure 5-7 (P-wave velocity), Figure 5-8 (seismic impedance) and Figure 5-5 (formation density).

Conclusions

The widespread changes in horizon amplitudes observed between the baseline and M5 surveys illustrate the difficulty of conducting terrestrial based 4D seismic surveys, where complex static corrections, intricate velocity variations in the shallow subsurface and a plethora of unrepeatable noise sources exist. The 1.85% change in seismic impedance and ~8% change in amplitude predicted by fluid replacement modeling are well below the ~15% noise component of the baseline and M5 survey spectrums (Figure 4-1). Therefore, it may be concluded that the signal-to-noise ratio of these surveys is insufficient for quantitative interpretation of supercritical CO_2 effect on seismic response at the reservoir level. Furthermore, amplitude difference maps exhibit survey wide changes in amplitude, with no distinct injection related difference limited to the vicinity of the CO2-I #1 well (Figure 6-5). Reprocessing of the surveys may remedy this problem, but as the data was acquired without a phase-locker, phase correction will be impossible and there will likely be little to no improvement in data quality resulting from reprocessing of the surveys.

The workflow put forth here is valid for data with a sufficiently high signal-to-noise ratio, or more specifically, the signal containing the fluid response in the reservoir is greater than the unrepeatable noise between baseline and monitor surveys. Unfortunately, this was not the case for the data acquired over the course of the Hall-Gurney CO_2-injection pilot program. In spite of successfully detuning the data, the interpretability was not improved because the unrepeatable noise in the baseline and M5 surveys is greater than the signal containing the fluid response in the reservoir. These results support the conclusion made by Raef et al. (2005a), that a non-differencing approach is necessary for identifying fluid response in the data collected during the Hall-Gurney CO_2-injection pilot program as a result of residual difference in time, phase,

amplitude and frequencies between the baseline and monitor surveys after cross-equalization. This workflow should be tested on data unaffected by these issues to assess its ability to decouple tuning and fluid responses in seismic data.

The future of CO_2 injection in the state of Kansas is promising, with recently implemented tax incentives likely to catalyze new injection programs. Monitoring programs seeking to track injected CO_2 utilizing reflection seismology will likely be challenged by a small fluid response and tuning effect overriding the fluid response, as many of these programs are likely to target the thinly bedded carbonates of the Lansing-Kansas City and Arbuckle Groups. Provided that the data is collected in a manner that preserves phase and amplitudes between surveys, these programs will likely benefit from utilizing a variation of the workflow presented in this study.

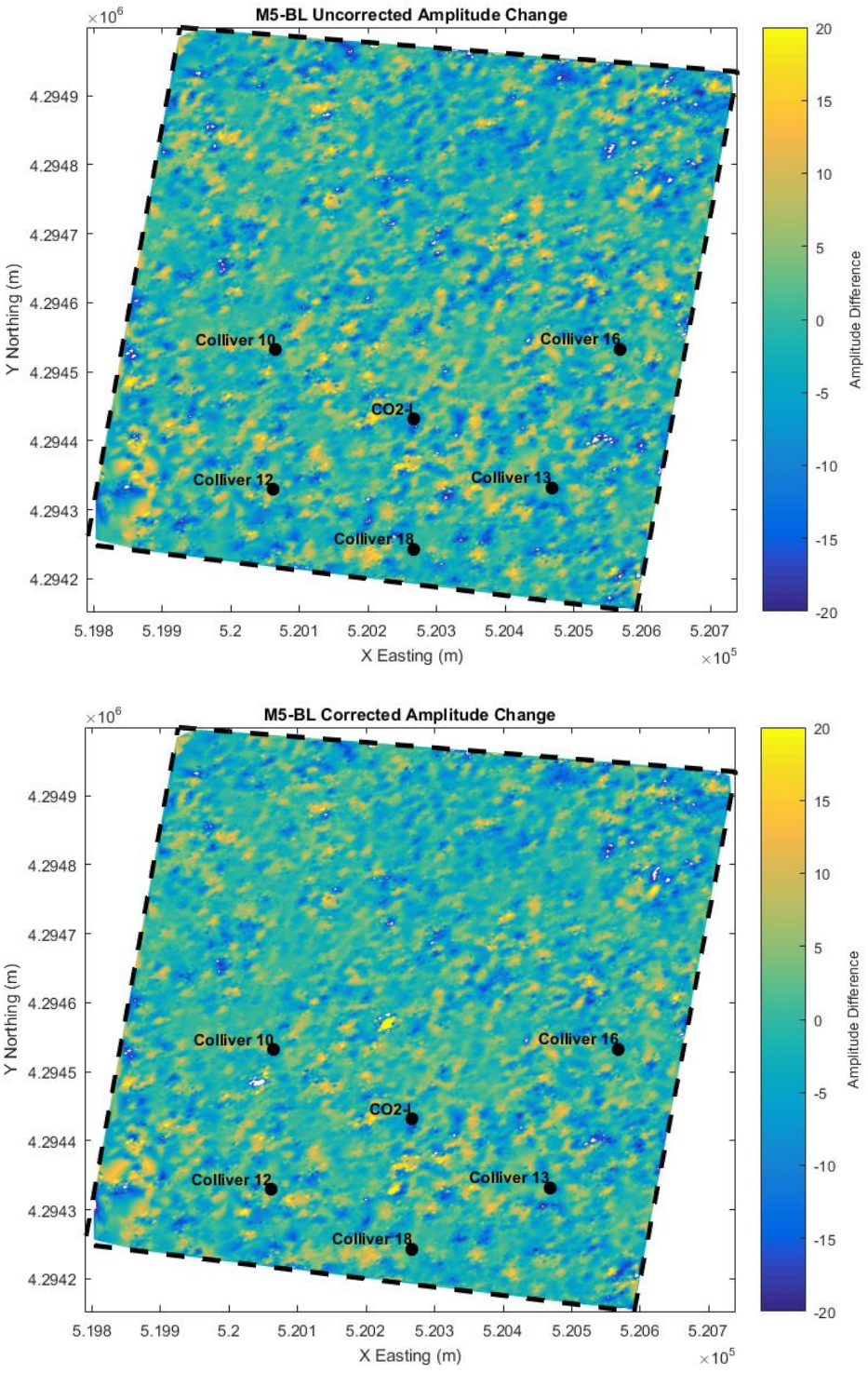

Figure 6-5: Amplitude difference maps depicting how amplitudes on the LKC top horizon have changed between the M5 and baseline surveys ($M5_{amplitudes} - BL_{amplitudes}$) before and after applying the tuning correction. Holes in the data and areas where amplitudes are over corrected correspond with zones where polarity reversals resulted in negative isochron values (which were removed) or zones of incoherency where the LKC top horizon could not be tracked. Notice that there is no distinct injection related amplitude difference that is limited to the vicinity of the CO2-I well.

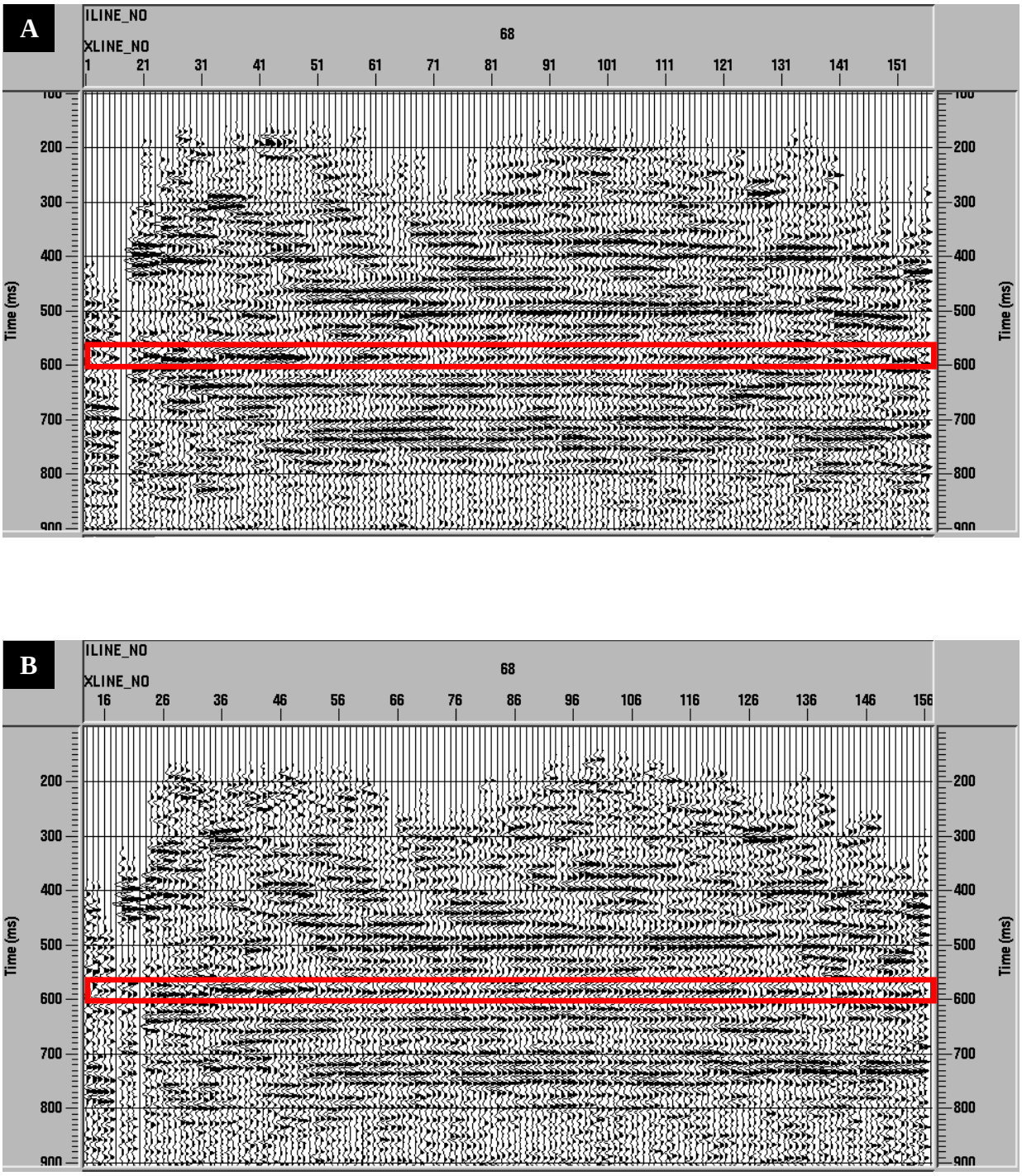

Figure 6-9: Cross-sections on inline 68 from the baseline (A) and M3 (B) surveys with no tuning correction applied. The reservoir is enclosed within the red box. Notice that supercritical CO_2 injection has increased the coherency of the LKC reflectors in the M3 survey after about 7 months of supercritical CO_2 injection.

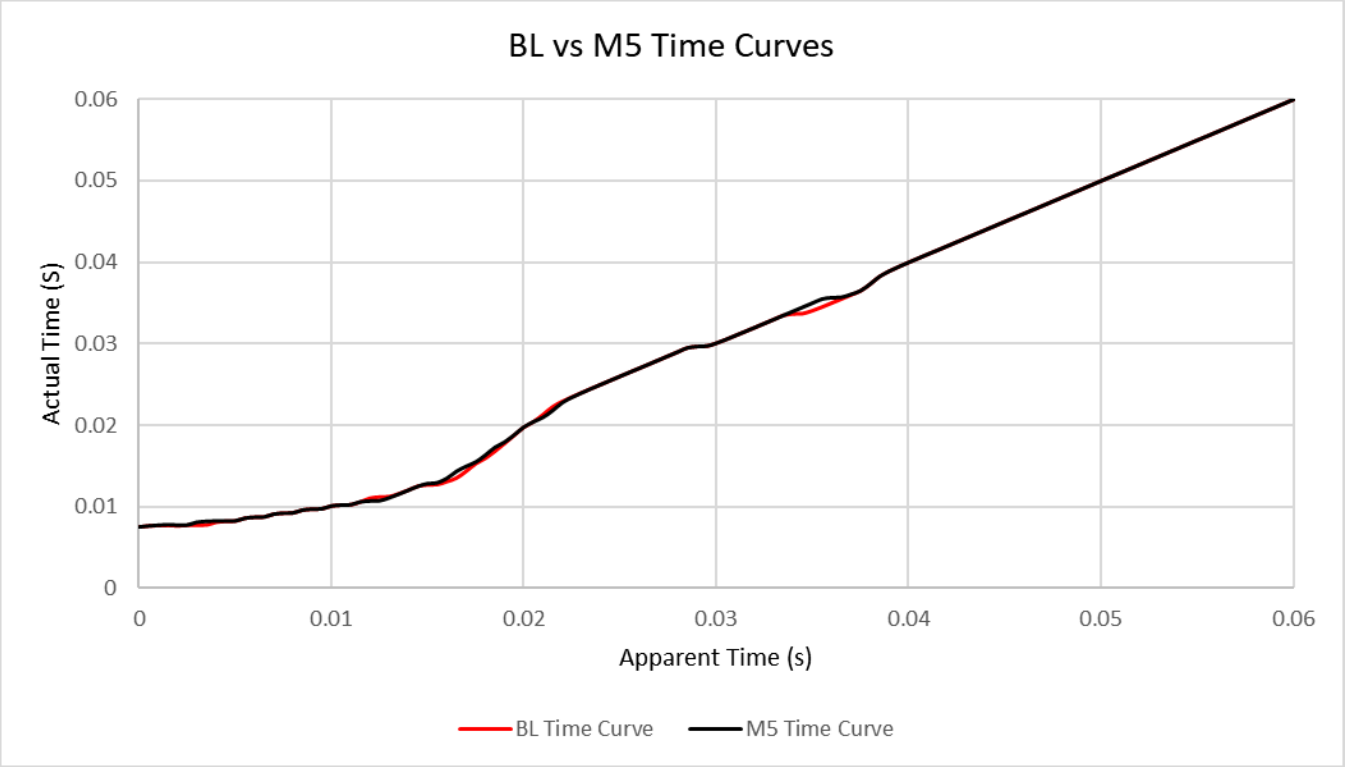

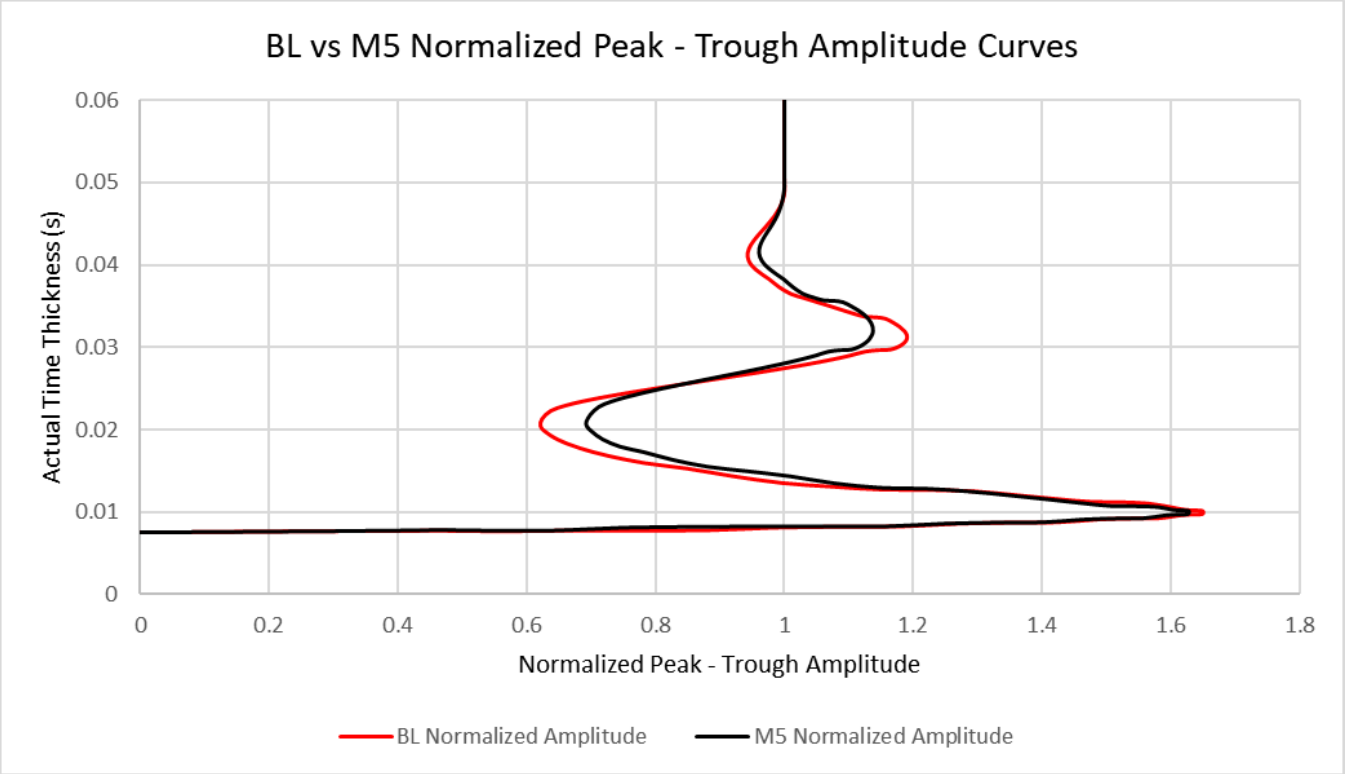

Figure 6-10: (A) Time thickness curves and (B) normalized peak - trough amplitude curves for the baseline and M5 surveys. These are the same curves in Figure 4-8 and are the result of convolving extracted wavelets with the reflection coefficient series of a wedge model. Differences between the tuning curves for the baseline and M5 survey suggest that supercritical CO_2 in the reservoir has affected the tuning effect at the reservoir level of the monitor survey.

References

Agile Geoscience. 2011. Tuning geology. Retrieved from: http://www.agilegeoscience.com/blog/2011/7/8/tuning-geology.html (accessed 3 May 2018)

Aveseth, P., Mukerji, T., and Mavko, G. 2005. Quantitative seismic interpretation applying rock physics tolls to reduce interpretation risk. Cambridge University Press. 4th printing 2013.

Arts, R., El Sayed, R., Van Der Meer, L., Eiken, O., Ostmo, S., Chadwick, A., Kirby, G., and Zinszner, B. 2002. Estimation of the mass of injected CO_2 at Sleipner using time-lapse seismic data. EAGE 64th Conference & Exhibition, 27-30 May 2002, Florence, Italy.

Baars, D.L., Watney, W.L., Steeples, D.W., and Brostuen, E.A. 1993. Petroleum: a primer for Kansas. Kansas Geological Survey, Education Series 7.

Byrnes, A.P, Franseen, E.K., Watney, W.L., and Dubois, M.K. 2003. The role of moldic porosity in Paleozoic Kansas reservoirs and the association of original depositional facies and early diagenesis with reservoir properties. Kansas Geological Survey Open File Report 2003-32.

Byrnes, A.P., Bhattacharya, S., Daniels, J.R., Victorine, J., and Stalder, K. 2011. Evaluating the influence of pore architecture and initial Saturation on wettability and relative permeability in heterogeneous, shallow-shelf carbonates. Oil and Natural Gas Technology, DOE NETL Office of Fossil Energy, project report.

Byrnes A.P., Watney, W.L., Guy, W.J., and Gerlach, P. 2000. Oomoldic reservoir of Central Kansas: controls on porosity, permeability, capillary pressure and architecture. AAPG Annual Convention, New Orleans, LA. AAPG Search and Discovery Article #90914

Carr, T.R., Merriam, D.F., and Bartley, J.D. 2005. Use of relational databases to evaluate regional petroleum accumulation, groundwater flow, and CO2 sequestration in Kansas. AAPG Bulletin, v. 89, no. 12, December, p. 1607-1627.

DOE. 2019. May 2019 monthly energy review. U.S. Energy Information Administration Monthly Energy Reviews, DOE/EIA-0035(2019/5).

Dubois, M.K., Byrnes, A.P., and Watney, W.L. 2001. Field development and renewed reservoir characterization for CO2 flooding of the Hall-Gurney Field, Central Kansas. AAPG Annual Convention, Denver, CO. AAPG Search and Discovery Article #90906.

Google Earth V 7.1.5.1557. (4 September 2013). Tongue of the Ocean, Bahamas. 23°16'11.91"N, 77° 9'44.71"W, Eye alt 19545 feet. Image Landsat 2015. http://www.earth.google.com (29 November 2015).

Higley, D.K. 1995. Cambridge Arch/Central Kansas Uplift Province (053). 1995 national assessment of United States oil and gas resources – results, methodology, and supporting data. U.S. Geological Survey Digital Data Series 30.

Hirsche, K. 2006. A personal perspective on the past, present and future of time-lapse seismic monitoring. Recorder, 31.

Holm, L.W., and Josendal, V.A. 1974. Mechanism of oil displacement by carbon dioxide: Journal of Petroleum Technology, Transaction AIME 257, December 1974, p. 1427–1438.

Jarrell, P.M., Fox, C.E., Stein, M.H., and Webb, S.L. 2002. Practical aspects of CO2 flooding: Richardson, Tex., Society of Petroleum Engineers Monograph Series, 22, p. 220.

Kansas Geological Survey (KGS). 2011. Oils and gas wells and fields; interactive oil and gas well maps. Retrieved from: http://maps.kgs.ku.edu/oilgas/index.cfm (accessed 19 March 2018)

Kelly, L. 2014. An investigation into the effects and implications of gamma radiation on organic matter, crude oil, and hydrocarbon generation. Kansas State University MS Thesis.

Krehel, A. 2014. Investigation of time-lapse 4D seismic tuning and spectral responses to CO2-EOR for enhanced characterization and monitoring of a thin carbonate reservoir. Kansas State University MS Thesis.

Martin, F.D., and Taber, J.J. 1992. Carbon dioxide flooding: Journal of Petroleum Technology, April, p. 396–400.

Merchant, D.H. 2010. Life beyond 80—A look at conventional WAG recovery beyond 80 % HCPV injection in CO2 tertiary flood: SPE 139516, presented at the SPE International Conference on CO2 Capture, Storage, and Utilization, New Orleans, La., U.S.A., November 10–12, p. 14.

Merriam, D.F. 1963. The geologic history of Kansas. Kansas Geological Survey Bulletin 162.

Miller, R.D., Raef, A.E., Byrnes, A.P., and Harrison, W.E. 2007. 4-D high-resolution seismic reflection monitoring of miscible CO2 injected into a carbonate reservoir. Final Report, September 2007.

Mougin, P., Rasolofosaon, P., and Zinsner, B. 2002. Petroacoustics of poorly consolidated reservoir rocks saturated with CO2/methane/brine mixtures. SACS European Research Project, work package 7, Institut Français du Pétrole (IFP).

NETL. 2010. Field demonstration of carbon dioxide miscible flooding in the Lansing Kansas City formation, central Kansas.

Newell, K.D., Watney, W.L., Cheng, S.W.L., and Brownrigg, R.L. 1987. Stratigraphic and spatial distribution of oil and gas production in Kansas. Kansas Geological Survey, Subsurface Geology Series 9.

Ohl, D., and Raef, A. 2014. Rock formation characterization for carbon dioxide geosequestration: 3Dseismic amplitude and coherency anomalies, and seismic petrophysical facies classification, Wellington and Anson-Bates Fields, Kansas, USA. Journal of Applied Geophysics, v. 103, p. 221-231.

Palaz, I., and Marfurt, K.J. 1997. Carbonate seismology: an overview. In: Carbonate Seismology, I. Palaz and K.J. Marfurt (Eds.), Geophysical Development Series No. 6, SEG, Tulsa, OK.

Perrin, J. 2016. Stripper wells accounted for 10% of U.S. oil production in 2015. Energy Information Administration Today in Energy. Retrieved from: https://www.eia.gov/todayinenergy/detail.php?id=26872 (accessed 13 October 2019)

Raef, A.E., Miller, R.D., Byrnes, A.P., and Harrison, W.E. 2004. 4D seismic monitoring of the miscible CO2 flood of Hall-Gurney Field, Kansas, U.S. The Leading Edge, 23.

Raef, A.E., Miller, R.D., Byrnes, A.P., Franseen, E.K., Watney, W.L., and Harrison, E.H. 2005a. A new approach for weak time-lapse anomaly detection using seismic attributes: geology and production data integrated monitoring of miscible EOR-CO2 flood in carbonates. SEG Annual Meeting, Houston, TX.

Raef, A.E., Miller, R.D., Byrnes, A.P., and Harrison, W.E. 2005b. Rock physics and seismic modeling guided application of 4D-seismic attributes to monitoring enhanced oil recovery CO2-flood in a thin carbonate reservoir, Hall Gurney Field, Kansas, U.S.A. 108, AAPG Annual Meeting, Calgary, Alberta, Canada. AAPG Search and Discovery Article #90039.

Sarg, J.F., and Schuelke, J.S. 2003. Integrated seismic analysis of carbonate reservoirs: from the framework to the volume attributes. The Leading Edge, 22.

Sheriff, R.E. 1977. Limitations on resolution of seismic reflections and geologic detail derivable from them. AAPG Memoir 26.

Simm, S., and Bacon, M. 2014. Seismic amplitude and interpreter's handbook. Cambridge University Press. 4th printing 2016.

Skirius, C., Nissen, S., Haskell, N., Marfurt, K., Hadley, S., Ternes, D., Michel, K., Reglar, I., D'Amico, D., Deliencourt, F., Romero, T., D'Angelo, R., and Brown, B. 1999. 3-D seismic attributes applied to carbonates. The Leading Edge, 3.

Stalkup, F.I., Jr. 1983. Status of miscible displacement: Journal of Petroleum Technology, April, p. 815–826.

Stalkup, F.I., Jr. 1984. Miscible displacement: Dallas, Tex., Society of Petroleum Engineers of AIME, SPE Monograph Series, ISBN 0-89520-319-7, p. 204.

Verma, M.K. 2015. Fundamentals of Carbon Dioxide-Enhanced Oil Recovery (CO2-EOR)—A Supporting Document of the Assessment Methodology for Hydrocarbon Recovery Using CO2-EOR Associated with Carbon Sequestration, U.S. Geological Survey Open-File Report 2015-1071.

Walker, G., and Parr, R. 2007. Time-lapse seismic: History to prediction. DEVEX Aberdeen, 2007. DOI: 10.13140/2.1.1518.8167

Wang, Z., and Nur, A. 1992. Elastic wave velocities in porous media: a theoretical recipe. SEG Geophysics Reprint Series, v. 2, no. 10.

Watney, W.L. 1994. Depositional sequence analysis and sedimentologic modeling for improved prediction of Pennsylvanian reservoirs. Final Report, U.S. DOE Contract DOE/BC/14434-13.

Watney, W.L. 2015. Reservoir lithofacies and their recent analogs. AAPG Education Course: Petrophysical Analysis and Integrated Approaches to the Study of Carbonate Reservoirs. April 21-23, 2015. Austin, TX.

Watney, W.L., Franseen, E.K., Byrnes, A.P., Miller, R., Raef, A.E., Reeder, S.L., and Rankey, E.C. 2006. Characterization of seismically-imaged Pennsylvanian ooid shoal geometries and comparison with modern. AAPG Annual Convention, Houston, TX. Search and Discovery Article #20038.

Widess, M.B. 1973. How thin is a thin bed? Geophysics, 38, No. 6.

Xu, S., and Payne, M.A. 2009. Modeling elastic properties in carbonate rocks. The Leading Edge, 28.

Yellig, W.F., and Metcalfe, R.S. 1980. Determination and prediction of CO2 minimum miscibility pressure: Society of Petroleum Engineers, JPT, January, p. 160–168.

Appendix A - Flowchart Legend

The following is to be used as a reference for following the flowcharts in Appendix B and Appendix C:

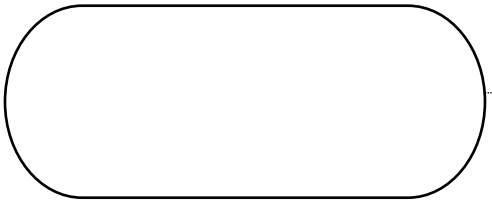

Start/End operations

Preparation step

Process/Calculation

Continue

Appendix B - Horizon Detuning Workflow as Implemented in MATLAB

Start:

1. Read in tuning curves from wedge model (exported from IHS Kingdom)
    a. Actual Time vs Apparent Time Curve
    b. Actual Time vs Normalized Peak-Trough Amplitude
2. Read in isochron horizon (in the format of: X, Y, Isochron Values)
3. Read in amplitude horizon (in the format of: X, Y, Z, Amplitude Values)

Remove invalid values from imported data:

- Amplitudes with values of 1e+30 (or other value that seismic interpretation software uses to denote invalid values)
- Negative isochron values

Interpolate isochron horizon values the XY grid of the amplitude horizon:

- This step accounts for the possibility that the isochron and amplitude horizons may have been exported utilizing different grids and allows for data exported from different software platforms to be integrated

Interpolate isochron horizon values onto the Apparent Time vs Actual Time curve (Figure 6-10) from the wedge model:

- This step allows for "Actual Time" values to be obtained for every isochron horizon value, which constitute the detuned isochron horizon values

Interpolate corrected (detuned) isochron horizon values onto the Actual Time vs Normalized Peak-Trough Amplitude curve (Figure 6-10):

- This step allows for amplitude correction factors to be obtained for every isochron value
- As a consequence of interpolating the isochron horizon to the amplitude horizon XY grid, the amplitude correction factors obtained in this step for isochron values will align with the amplitude values on the amplitude horizon

Correct amplitude values by applying Equation 4-1:

$$A_c = A_H - \frac{1}{2}\left[(\tau_A - 1) * \frac{A_H}{\tau_A}\right]$$

- $A_c =$ detuned amplitudes, which constitute the corrected amplitude horizon values
- $A_H =$ amplitude horizon values (uncorrected amplitudes)
- $\tau_A =$ amplitude correction factor, obtained in the previous step from the Normalized Peak-Trough Amplitude curve
- The second term of this equation is multiplied by $\frac{1}{2}$ because the correction factors obtained in this step are determined from peak-trough amplitudes while the amplitudes in the amplitude horizon are defined from an origin of zero

End:

- Write detuned isochron file in the format of X, Y, Z, Isochron Values
    - The corrected isochron horizon possesses the same XY grid and Z values as the input amplitude horizon
- Write detuned amplitude horizon in the format of X, Y, Z, Amplitude Values

Appendix C - Fluid Replacement Modeling Workflow as Implemented in MATLAB

Start:

- Read in initial variables defined manually by the user (see Table 4-3 and Table 4-4)
  - K_{rock}, K_{brine}, K_{oil}, K_{CO_2}, ϕ, S_w, ρ_{rock}, ρ_{b1}, ρ_{brine}, ρ_{oil}, ρ_{CO_2}, μ_{rock}, V_{p1},V_{s1}
  - CO_2 saturation step
    - A CO_2 saturation step of 0.1 was used to produce following figures: Figure 5-5, Figure 5-6, Figure 5-7, Figure 5-8 and Figure 6-4

Calculate the bulk density of the initial reservoir fluid:

$$\rho_{f1} = \rho_{brine} S_w + \rho_{oil}(1 - S_w)$$

Calculate the bulk density of CO_2 saturated reservoir fluid for each CO_2 saturation step:

$$\rho_{f2} = \rho_{brine}\left(S_w - S_{CO_2}\right) + \rho_{oil}(1 - S_w) + \rho_{CO_2} S_{CO_2}$$

Calculate bulk reservoir density for each CO_2 saturation step:

$$\rho_{b_2} = \rho_{f2} + \rho_{rock}(1 - \phi)$$

Calculate initial reservoir bulk modulus:

$$K_{sat1} = \rho_{b1}\left(V_{p1}^2 - \frac{4}{3}V_{s1}^2\right)$$

Calculate reservoir shear modulus:

$$\mu_{sat1} = \mu_{sat2} = \rho_{b1} V_{s1}^2$$

Calculate the bulk modulus of the initial reservoir fluid:

$$K_{f1} = \left(\frac{1 - S_w}{K_{oil}} + \frac{S_w}{K_{brine}}\right)^{-1}$$

Calculate the bulk modulus of the CO_2 saturated reservoir fluid for each CO_2 saturation step:

$$K_{f2} = \left[\frac{1 - \left(S_w - S_{CO_2}\right)}{K_{oil}} + \frac{S_w - S_{CO_2}}{K_{brine}} + \frac{S_{CO_2}}{K_{CO_2}}\right]^{-1}$$

Calculate the bulk density of CO_2 saturated reservoir for each CO_2 saturation step:

$$K_{sat2} = \frac{K_{mineral}}{\left[\frac{K_{sat1}}{K_{mineral} - K_{sat1}} - \frac{K_{f1}}{\phi\left(K_{mineral} - K_{f1}\right)} + \frac{K_{f2}}{\phi\left(K_{mineral} - K_{f2}\right)}\right]^{-1}}$$

Calculate new P-wave velocities for each CO_2 saturation step:

$$V_{p2} = \sqrt{\frac{K_{sat2} + \frac{4}{3}\mu_{sat2}}{\rho_{b2}}}$$

Calculate new S-wave velocities for each CO_2 saturation step:

$$V_{s2} = \sqrt{\frac{\mu_{sat2}}{\rho_{b2}}}$$

Calculate new seismic impedance for each CO_2 saturation step:

$$I = \rho_{b2} V_{p2}$$

Calculate percent change in reservoir bulk properties:

$$\Delta V_p = \left|\frac{V_{p1} - V_{p2}}{V_{p1}}\right| \times 100$$

$$\Delta I = \left|\frac{I_1 - I_2}{I_1}\right| \times 100$$

$$\Delta \rho_{b2} = \left|\frac{\rho_{b1} - \rho_{b2}}{\rho_{b1}}\right| \times 100$$

End:

- Display graphs:
  - Reservoir Bulk Density vs CO_2 Saturation (Figure 5-5)
  - Reservoir Bulk Modulus vs CO_2 Saturation (Figure 5-6)
  - P-Wave Velocity vs CO_2 Saturation (Figure 5-7)
  - Seismic Impedance vs CO_2 Saturation (Figure 5-8)
  - Reservoir Bulk Properties (Percent Change) vs CO_2 Saturation (Figure 6-4)